Document Version
Final published version

Citation (APA)
Sun, P., Huang, C., Zhang, H., Qiu, Z., Geng, S., Sun, K., & Hao, X. (2026). Enhancing operational resilience of standalone photovoltaic-electrolyzer systems: A comparative analysis of single- and dual-stage power interface architectures. *Applied Energy*, *415*, Article 127888. https://doi.org/10.1016/j.apenergy.2026.127888

Applied Energy 415 (2026) 127888

Contents lists available at ScienceDirect

Applied Energy

journal homepage: www.elsevier.com/locate/apen

Enhancing operational resilience of standalone photovoltaic-electrolyzer systems: A comparative analysis of single- and dual-stage power interface architectures

Pingyang Sun[a], Chunjun Huang[b], Hanwen Zhang[c], Zihang Qiu[d], Shu Geng[e], Kaiwen Sun[a,*], Xiaojing Hao[a]

[a] *School of Photovoltaic and Renewable Energy Engineering, UNSW Sydney, Sydney, NSW, 2052, Australia*
[b] *Electrical Sustainable Energy Department, Delft University of Technology, Delft, Netherlands*
[c] *Department of Electronics and Electrical Engineering, University of Bath, Bath, UK*
[d] *School of Electrical Engineering & Telecommunications, UNSW Sydney, Sydney, NSW, 2052, Australia*
[e] *School of Chemical Engineering, UNSW Sydney, Sydney, NSW, 2052, Australia*

HIGHLIGHTS

- Analysis of single & dual dc/dc converters in standalone PV-electrolyzer systems.
- Study of low-power-ride-through strategies during PV power insufficiency.
- Simulation validation of system configurations and control schemes.
- Experimental validation using a GaN-based converter prototype.

ARTICLE INFO

Keywords:
Photovoltaic (PV)
Electrolyzer
Standalone PVEC system
Dc/dc converter
Low power ride-through (LPRT)

ABSTRACT

Off-grid power delivery from photovoltaic (PV) systems to electrolyzers serves as a key pathway toward sustainable green hydrogen production, with the PV output voltage adapted to the electrolyzer operating voltage by dc/dc converters. However, a systematic understanding of the performance trade-offs between different converter architectures and their associated control strategies is still lacking, particularly for ensuring robust operation under intermittent solar conditions. This paper presents a systematic comparative study of single- and dual-stage dc/dc converter architectures for standalone PV-electrolyzer (PVEC) systems. The study investigates the fundamental control trade-offs, comparing the single-stage's rigid electrolyzer-following operation with the dual-stage's superior flexibility in providing direct electrolyzer current regulation. To enhance operational resilience, two distinct low power ride-through (LPRT) strategies are proposed and analyzed for the dual-stage configuration, ensuring stable power delivery during significant solar power reductions. The feasibility and performance of the proposed architectures and control strategies are validated through both 5 kW system simulations and experiments on a 200 W GaN-based hardware prototype. The results demonstrate that while the single-stage architecture is viable for small-scale systems, the dual-stage configuration's enhanced control flexibility and scalability are essential for large-scale, storage-ready PVEC applications.

1. Introduction

Standalone photovoltaic-electrolyzer (PVEC) systems are a promising solution for decentralized green hydrogen production, especially in remote areas, by directly converting solar energy into storable hydrogen to enhance energy autonomy and reduce fossil fuel reliance [1,2]. Compared to grid-connected configurations, these systems offer a simpler energy conversion pathway with lower transmission losses and reduced complexity [3,4]. The global drive for decarbonization is accelerating the deployment of such systems, as reflected by an increasing number of practical projects demonstrating their scalability, including

---

* Corresponding author.
Email address: kaiwen.sun@unsw.edu.au (K. Sun).

https://doi.org/10.1016/j.apenergy.2026.127888
Received 30 January 2026; Received in revised form 19 March 2026; Accepted 10 April 2026

Nomenclature

Converter Parameters

θ_n	n^{th} phase
A_{nh}	Amplitude of the h^{th} harmonic of the n^{th} phase
$D_{i,ref}$, $\Delta D_{i,ref}$	Output in current balance controller, current correction value
$D_{mppt,ref}$, $D_{mv,ref}$, $D_{ely,ref}$	Duty cycles in control loops of MPPT, middle dc-link voltage, electrolyzer current
G_{mppt}, G_{inner}, G_{ely}	Controller gains of MPPT, inner current, electrolyzer current
I_{op}, $I_{op,ref}$	Phase current, average phase current
i_o, i_n	Total ripple current, ripple current of the n^{th} phase
N	Number of phases

Electrolyzer Parameters

α_a, α_c	Charge transfer coefficients for anode and cathode
$\dot{n}_{H_2}^{in}$	Hydrogen production flow
η_F	Faraday efficiency
σ_{mem}	Proton conductivity
A_{cell}	Electrolyzer cell active area
C_{dl}, C_d	Double-layer capacitance
$C_{O_2,ch}$, $C_{H_2,ch}$	Oxygen and hydrogen concentrations at the channel interface
$C_{O_2,mem}$, $C_{H_2,mem}$	Oxygen and hydrogen concentrations at the membrane interface
j, $j_{0,a}$, $j_{0,c}$	Current density, exchange current densities at the anode and cathode
N_{cell}	Number of cells in the electrolyzer
P_{ely}, V_{ely}, I_{ely}	Electrolyzer power, voltage, current
R, F	Gas constant, Faraday constant
r_1, r_2, c_1, c_2	Scaling coefficients
R_m, R_{act}, R_d	Emulated resistance relevant to overpotentials
t_{mem}	Membrane thickness
V_{act}, V_{ohm}, V_{conc}	Electrolyzer activation, ohmic, concentration overpotentials
V_{cell}, I_{cell}	Electrolyzer cell voltage, cell current
V_{rev}	Electrolyzer reversible voltage
V_{stack}, I_{stack}	Electrolyzer stack voltage, stack current
z	Number of transfer electrons

PV Parameters

I_{ph}, I_0, I_{sc}	Light-generated current, diode reverse saturation current, short-circuit current
P_{mp}, V_{mp}, I_{mp}	PV maximum power, voltage at maximum power, current at maximum power
q, n, k_B	Elementary charge, diode ideality factor, Boltzmann constant
R_s, R_{sh}	Series resistance, shunt resistance
α, β	Temperature coefficient of short-circuit current, temperature coefficient of maximum power
δ, ε	Perturbation step under P&O MPPT, threshold of power change
ΔP_{pv}, ΔV_{pv}	PV power change, voltage change
G, T	Solar irradiance, PV cell temperature
P_{pv}, V_{pv}, I_{pv}	PV power, voltage, current

developments in Australia [5], Japan [6], and China [7,8]. One representative example is the 600 MW off-grid green hydrogen project in the Pingshuo mining area of China [8], which integrates large-scale renewable generation with on-site hydrogen production to replace fossil-based hydrogen in coal-to-ammonia processes. Its first phase integrates a 100 MW PV plant, multiple alkaline electrolyzers, and hydrogen storage, and aims to produce approximately 32.6 million Nm^3 of green hydrogen annually.

PVEC systems operating in off-grid mode can be broadly categorized into: 1) systems incorporating energy storage systems (ESSs), and 2) systems operating without ESSs. Incorporating an ESS (e.g., batteries [9]) into standalone PVEC systems can effectively mitigate the inherent mismatch between fluctuating solar generation and electrolyzer load demand, thereby ensuring continuous and stable hydrogen production. Such a configuration is particularly suited to applications with high reliability requirements, including hydrogen refueling stations and chemical industries such as large-scale ammonia synthesis. However, this approach also introduces additional complexities [1,2,10], including higher capital and operational expenditures, increased maintenance needs, and potential lifetime limitations of batteries. These issues can be especially pronounced in harsh or remote environments where accessibility and servicing are challenging [11]. In contrast, systems operating without ESSs provide a simpler and more cost-effective architecture, making them attractive where continuous hydrogen supply is not essential or where investment constraints dominate. By directly coupling PV modules to electrolyzers, typically through one or more stages of dc/dc converters, such systems avoid the energy losses and degradation pathways associated with intermediate storage cycles [4,12]. This configuration is well suited for small-scale demonstration projects, flexible applications, and off-grid sites where intermittent hydrogen production is acceptable and reduced upfront cost and simplified operation are prioritized. In addition, in space-constrained environments where deploying large-scale ESSs is impractical, direct coupling provides a compact and viable alternative [3,12].

The deployment of standalone PVEC systems relies on advanced electrolyzer technologies, with development progressing along four main technologies: alkaline (ALK) electrolysis, proton exchange membrane electrolysis (PEM), solid oxide electrolysis cell (SOEC), and anion exchange membrane electrolysis (AEM) [13,14]. ALK electrolysis, a mature and cost-effective technology, remains a mainstream choice, particularly in China where companies like Sungrow Hydrogen and LONGi Hydrogen are deploying large-scale units [1,15,16]. PEM electrolysis, known for its high current density, rapid response, and compactness, is gaining significant attention globally, with Europe and the US leading in deployment and manufacturing by companies like Thyssenkrupp, NEL, Siemens Energy, Plug Power, and Cummins [4,17,18]. SOEC and AEM technologies are still at the research or early demonstration stage, with limited industrial involvement and low commercialization. Direct coupling in standalone PVEC systems, especially without energy storage, imposes stringent requirements on electrolyzers: efficient handling of fluctuating PV power, wide load-following, and sustained dynamic performance. Therefore, PEM's rapid response and good partial load capabilities make it suitable for such scenarios [4].

Extensive research has focused on improving the overall performance and economic viability of PVEC systems, with particular emphasis on system-level planning, energy management, and techno-economic optimization. A dominant theme in this body of work is the sizing and configuration of PV arrays and electrolyzers to balance hydrogen yield, system efficiency, and cost. Early studies explored how geographical and climatic conditions influence optimal system sizing, demonstrating that technically optimal configurations do not necessarily yield the minimum hydrogen cost [19]. Building on this, subsequent studies employed advanced heuristic optimization methods e.g. multi-level genetic algorithms, and direct PV–electrolyzer coupling strategies, to jointly optimize hydrogen production, system losses, and component configurations [20,21]. To improve practical feasibility, later work incorporated techno-economic uncertainty through robust optimization frameworks, highlighting the sensitivity of optimal designs to financial assumptions and operating conditions [22]. More recent studies have further refined capacity-configuration optimization for PV-battery-electrolysis hybrid systems by incorporating dynamic electrolyzer efficiency, technology cost-learning effects, and PV-output uncertainty, showing that these factors can materially affect both optimal sizing and lifecycle cost [23]. While broader techno-economic assessments have further emphasized the role of regional factors and component choices [11,24], fundamental bottom-up analyses have paralleled this by comparing architectures to assess integration efficiency under dynamic conditions [25]. This diversity of planning and economic optimization approaches has been systematically categorized in recent reviews [3]. Despite these advances, most existing studies still assess PVEC systems primarily from a planning, sizing, or steady-state performance perspective, with comparatively limited attention to converter-level dynamic interactions, control flexibility, and transient resilience under highly variable solar input.

The above limitation has motivated growing interest in moving beyond static techno-economic optimization toward dynamic, control-relevant assessment of standalone PVEC systems. From a power-electronics perspective, recent reviews have emphasized that the converter interface is a key enabler for improving controllability, efficiency, and source-load matching in PV-hydrogen systems [26]. At the device level, a central challenge is the electrical mismatch between the PV source and the electrolyzer. Direct-coupling studies avoid full-power converter processing, but they tightly bind the electrolyzer operating point to the PV characteristic and therefore provide limited flexibility for independent PV-side and electrolyzer-side regulation [3,27]. To improve controllability, early converter-coupled studies employed single-stage buck interfaces in small-scale PVEC systems [28,29]. More recent studies have extended this line toward scalable single-stage interleaved or modularized buck converters for kW-level operation, mainly to improve current quality, voltage matching, and safe operation under varying conditions [30]. In parallel, advanced converter studies have further highlighted the importance of high step-down capability, low ripple, and improved dynamic robustness for electrolyzer applications [31,32]. Furthermore, a more flexible two-stage converter architecture using dc transformers with partial-power converter pre-regulators (PPC + DCX) has also been investigated [12]. This architecture allows for decoupling PV-side regulation (e.g., maximum power point tracking, MPPT) from electrolyzer-side regulation and improves efficiency in high-voltage-ratio applications.

Related studies have further shown that, under variable solar input, the challenge in standalone PVEC systems is not only efficient energy conversion but also maintaining stable source-load power matching over changing operating conditions. Recent studies have mainly addressed this power matching issue for standalone PVEC systems through supervisory curtailment or dynamic MPPT enhancement rather than converter-level ride-through design [33,34]. Other off-grid control studies have explored coordinated power allocation among multiple PEM electrolyzer operating states through multi-layer dc/dc interfaces, further illustrating the importance of dynamic control under fluctuating renewable energy sources (RES) [35]. By contrast, battery-assisted approaches can maintain more stable electrolyzer operation by buffering power deficits through storage, but at the cost of added system complexity and a different operating premise from standalone PVEC systems [36]. At a broader system level, architecture-oriented studies have compared direct, dc–dc, and ac or direct and indirect coupling options, highlighting distinct trade-offs in flexibility, losses, and controllability [37,38]. In addition, recent topology-comparison studies on electrolyzer power converters have further underlined the importance of structured comparison across converters, although these studies are not specifically focused on standalone PVEC systems [39].

As summarized in Table 1, recent studies have substantially expanded the understanding of standalone or closely related PVEC systems from power-interface architectures to selected dynamic control

Table 1

Representative studies on coupling architectures and control flexibility for standalone or closely related PVEC systems.

Ref.	System configuration	Power interface architecture[1]	Control flexibility	Architecture / mode comparison[2]	LPRT analysis[3]	Experimental test
[3,27]	PV–EC	Direct coupling / no converter	PV-following only	✓	✗	✗
[28]	PV–EC	Single-stage buck converter	PV-side regulation	✗	✗	✗
[29]	PV–EC	Single-stage buck converter	PV-side regulation	✗	✗	✗
[30]	PV–EC	Single-stage interleaved / modularized buck	PV-side regulation	✗	✗	✓
[31,32]	Electrolyzer-fed by RES	Advanced high step-down converter topologies	PV-side or converter-side regulation for dynamic current control	✗	✗	✓
[33]	PV–EC	Single-stage converter-coupled system	PV-side regulation	✗	✗	✓
[35]	PV–EC	Multi-layer dc/dc converter system	Coordinated electrolyzer-side power allocation	✗	✗	✗
[36]	PV–battery–EC	Battery-assisted indirect coupling with a dc/dc converter	Battery-buffered EC-side regulation	✗	✗	✓
[12]	PV–EC	Dual-stage (PPC + DCX)	Decoupled PV-side and EC-side regulation	✗	✗	✓
[37,38]	PV–EC	Direct / indirect / ac coupling	System-level architecture assessment only	✓	✗	✗
[39]	Electrolyzer converter systems	Multiple converter topologies	Topology-level comparison only	✓	✗	✗
[26]	PV-based hydrogen systems	Review of direct, dc/dc,ac-grid and dc-microgrid interfaces	Review-level taxonomy only	✓	✗	✗
This work	**PV–EC**	**Single-stage and dual-stage buck dc/dc**	**Single-stage: PV-side regulation; dual-stage: decoupled PV-side and EC-side regulation, with mode comparison[4]**	✓	✓	✓

[1] “Stage” refers only to the main power-conversion path from the PV source to the electrolyzer.

[2] “Architecture / mode comparison” indicates whether the cited study explicitly compares multiple power-interface architectures and/or distinct converter control modes, rather than investigating only a single fixed configuration.

[3] “LPRT analysis” refers to converter-level low-power ride-through analysis under abrupt solar power changes.

[4] In this work, the single-stage converter uses PV-side regulation, whereas the dual-stage converter enables two control modes: Mode 1 combines PV-side MPPT with dc-link regulation, and Mode 2 combines dc-link regulation with direct electrolyzer current regulation.

strategies. Nevertheless, three critical gaps remain. First, representative standalone PVEC studies are mostly limited to either direct coupling, single-stage converter design, or a specific dual-stage solution, while experimentally supported comparisons between single-stage and dual-stage converter architectures remain scarce [12,30]. Second, the control flexibility enabled by converter architecture has not been systematically clarified. Most direct-coupled and single-stage studies remain limited to PV-following or PV-side regulation [28,29], whereas dual-stage studies enable decoupled PV-side and electrolyzer-side regulation but do not systematically compare PV-priority and EC-priority regulation modes within a unified framework [12]. Third, under abrupt solar power deficits, battery-less studies mainly rely on supervisory curtailment or enhanced dynamic tracking, while battery-assisted studies absorb the deficit through storage [33,36]. Converter-level low-power ride-through (LPRT) strategies capable of preventing dc-link collapse through fast local electrical feedback remain insufficiently explored and experimentally validated. Addressing these gaps is essential for establishing reliable design and control guidelines for standalone PVEC systems.

To address the above gaps, this paper presents a detailed comparative study of converter architectures and control strategies for standalone PVEC systems. The main contributions are summarized as follows:

1. A systematic comparative design and analysis of both single-stage and dual-stage buck dc/dc converter configurations for standalone PVEC systems is carried out. This includes a quantitative assessment of transient behavior, operating flexibility, scalability, hydrogen production performance, electrolyzer system efficiency, and stable electrolyzer operation under solar power deficits, together with a direct comparison of the control functions uniquely enabled by the dual-stage architecture.
2. Two distinct LPRT strategies are proposed and analyzed for the dual-stage converter, namely current-reference reduction and control-mode switching. These strategies are developed to maintain safe and stable operation during abrupt solar power drops by mitigating source-load power deficits and preventing dc-link collapse. Representative results show that the control-mode-switching strategy can enable the system to settle to the new PV operating condition within less than 0.5 s, while the current-reference-reduction strategy maintains hydrogen production at 0.58–1.01 Nm^3/h with electrolyzer system efficiency up to 96.75%–97.12% under representative 50% irradiance reduction conditions.
3. Comprehensive validation is provided through detailed 5 kW simulations and experiments on a 200 W GaN-based hardware prototype, thereby demonstrating the feasibility, efficiency, and dynamic performance of the proposed converter topologies and control schemes under realistic operating conditions.

This work is organized as follows. Section 2 presents the system description and component-level modeling. Section 3 introduces the proposed converter configurations and control strategies, including the LPRT schemes. Section 4 provides the simulation-based comparative analysis. Section 5 presents the experimental validation results. Section 6 discusses potential improvements, technology-specific applicability, alternative converter solutions, and scalability considerations for practical deployment. Finally, Section 7 concludes the paper.

2. Configuration and modelling of standalone PV-electrolyzer (PVEC) systems

In off-grid PV-powered hydrogen production systems, a natural mismatch exists between PV modules and electrolyzers. PV arrays typically operate at relatively high voltage and low current, whereas electrolyzers present a low-voltage, high-current load due to their inherent V-I characteristics. For instance, in a 500 W system, a small-scale electrolyzer may require 10–20 V, while the maximum power point voltage of the PV module can reach 35–45 V. Therefore, the interconnection between the two components requires an efficient dc/dc conversion solution that can not only match the dynamics of the PV voltage, but also meet the electrolyzer's voltage and current requirements. At the kilowatt scale (e.g., a 5 kW system), the PV array may deliver 200–400 V depending on its configuration, while the electrolyzer stack still operates at only tens of volts but demands hundreds of amperes of current, since the hydrogen production rate is proportional to current density. Such significant disparity further highlights the need for proper dc/dc conversion solutions for standalone PVEC systems.

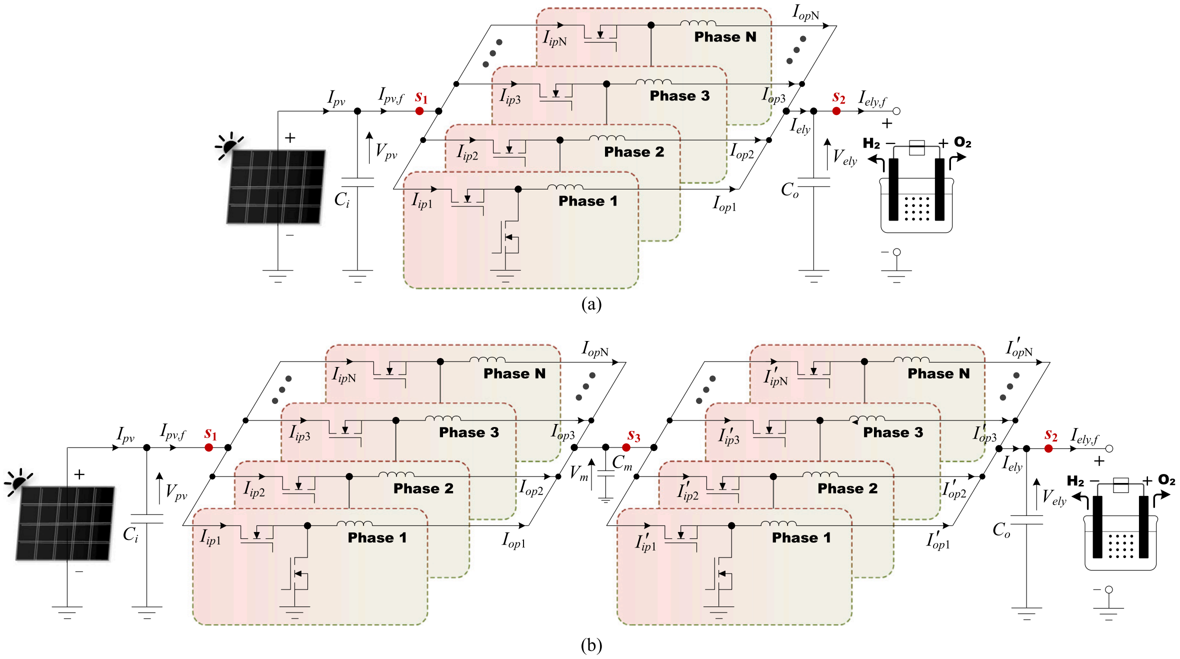

(a)

(b)

Fig. 1. Standalone PVEC system configurations: (a) PVEC system with single multiphase interleaved buck converter, and (b) PVEC system with dual multiphase interleaved buck converters.

Table 2
Comparison of single-stage and dual-stage converter architectures in standalone PVEC systems.

Aspect	Single-Stage Converter	Dual-Stage Converter
Control capability	Limited to one control degree of freedom	Additional control degrees of freedom (e.g. intermediate dc-link voltage regulation & electrolyzer current control)
Coupling	Strong coupling between PV and electrolyzer	Decoupling through intermediate dc-link
Duty cycle	Very low duty cycles may occur	Staged conversion alleviates the low duty cycle problem
Efficiency	Simpler structure with fewer components, potentially lower conduction loss	Lower efficiency due to the use of two converters
Scalability	Limited scalability for high-power systems	Improved scalability through modular and staged architecture
System complexity	Simple topology and control implementation	Higher system complexity and control design effort
Operational flexibility	Limited flexibility in system regulation	Greater flexibility in power regulation and system operation

Table 3
Comparison of ac-coupled and dc-coupled architectures in PVEC systems.

Aspect	Ac-coupled PVEC system	Dc-coupled PVEC system
Conversion efficiency	Lower efficiency due to multiple power conversion stages	Higher efficiency owing to reduced conversion stages
Control flexibility	PV and electrolyzer operate independently with separate control loops	Requires coordinated control between PV generation and electrolyzer operation
MPPT implementation	MPPT is implemented in the PV inverter independently of the electrolyzer	MPPT can be integrated with the dc/dc converter control in the PVEC interface
Electrolyzer operation control	Electrolyzer current is regulated through the rectifier or power management system	Electrolyzer current or voltage can be directly controlled through the dc/dc interface
System coupling	Weak coupling between PV generation and electrolyzer load	Strong coupling between source and load through the dc bus
System efficiency at low power	Additional conversion stages reduce efficiency at partial load conditions	Higher efficiency at partial load due to fewer conversion stages

Fig. 1 shows two adopted converter configurations of standalone PVEC systems, including single and dual interleaved buck converters. The detailed architecture comparison is presented in Table 2, while an additional comparison between the ac- and dc-coupled PVEC systems is provided in Table 3. In both cases, the interleaved structure employs multiple synchronous buck modules that share the total output current supplied to the electrolyzer. This interleaved structure enables a modular design where each phase utilizes the same power rating design that can be easily expanded to accommodate different power ratings. In the first configuration, a single dc/dc converter provides direct voltage conversion from the PV array to the electrolyzer. This tightly coupled structure simplifies the system and minimizes the number of conversion stages. However, as system power increases, the voltage difference between the PV array and the electrolyzer becomes more pronounced, resulting in very low duty cycles. This operating condition leads to higher power losses caused by circulating current, particularly when the duty cycle drops below 0.1, and narrows the power regulating range. To address this, optimized inductor design is required to maintain continuous current mode (CCM) operation and suppress current ripple in each phase.

In contrast, the second configuration adopts two interleaved buck converters. The PV output is first converted into an intermediate dc voltage V_m, and subsequently regulated to meet the electrolyzer voltage requirements through a staged conversion process. This staged conversion provides voltage decoupling, thereby mitigating the low duty cycle problem inherent in the single-converter design. Moreover, the dual-stage approach offers greater control flexibility and improved efficiency under varying operating conditions. This multi-phase and multi-stage configuration features reduced current ripple, enhanced scalability, and improved fault tolerance, making it an attractive solution for electrolyzer interfacing at larger scales.

2.1. PV modelling

Single-diode equivalent circuit is used to represent the PV system, which is widely adopted due to its balance between accuracy and simplicity [40]. It comprises a current source representing the photogenerated current, a diode accounting for the nonlinear I/V behavior, and both series and shunt resistances reflecting internal losses. The output current I_{pv} as a function of the terminal voltage V_{pv} is described:

$$I_{pv} = I_{ph} - I_0\left[e^{\dfrac{q(V_{pv} + I_{pv}R_s)}{nk_BT_K}} - 1 \right] - \frac{V_{pv} + I_{pv}R_s}{R_{sh}}, \tag{1}$$

where I_{ph} refers to the light-generated current, I_0 is the diode reverse saturation current, q is the elementary charge, R_s and R_{sh} are the series and shunt resistances, n is the diode ideality factor, k_B is Boltzmann constant (J/K), and T_K indicates the cell temperature in Kelvin. The photogenerated current I_{ph} is influenced by solar irradiance G and temperature, and is calculated as:

$$I_{ph} = \left[I_{sc,ref} + \alpha I_{sc,ref}(T - T_{ref})\right] \cdot \frac{G}{G_{ref}}, \tag{2}$$

where $I_{sc,ref}$ is the short-circuit current under standard test conditions, α is the temperature coefficient of the short-circuit current (%/°C), T_{ref} is the reference cell temperature (usually 25 °C), G is the actual solar irradiance (W/m^2), and G_{ref} is the reference irradiance at STC (1000 W/m^2).

To maximize energy extraction from the PV system, the widely adopted Perturb and Observe (P&O) [41] MPPT method is implemented. It perturbs the reference voltage $\Delta V_{pv} = V_{pv}(k) - V_{pv}(k-1)$, and observes the resulting power change $\Delta P_{pv} = P_{pv}(k) - P_{pv}(k-1)$. If power increases (3), the perturbation continues in the same direction; otherwise, it reverses (4). The P&O algorithm is also utilized in both the simulation and experiment of this paper, while the reference voltage is constrained within a predefined range ($V_{pv,\min} \le V_{pv,ref} \le V_{pv,max}$) to reduce oscillations near the MPP and enforce voltage limits for safe operation.

$$\begin{cases} \Delta V_{pv} > 0 \rightarrow V_{pv,ref} \leftarrow V_{pv,ref} + \delta \\ \Delta V_{pv} < 0 \rightarrow V_{pv,ref} \leftarrow V_{pv,ref} - \delta \end{cases}, \quad \text{if } \Delta P_{pv} > \varepsilon \,, \tag{3}$$

$$\begin{cases} \Delta V_{pv} > 0 \rightarrow V_{pv,ref} \leftarrow V_{pv,ref} - \delta \\ \Delta V_{pv} < 0 \rightarrow V_{pv,ref} \leftarrow V_{pv,ref} + \delta \end{cases}, \quad \text{if } \Delta P_{pv} < -\varepsilon \,, \tag{4}$$

where δ refers to the perturbation step, and ε is the threshold of power change.

2.2. Electrolyzer modelling

The study focuses on the PEM electrolyzer [Fig. 2(a)], given its commercial maturity and advantages (high current density, purity, fast dynamics) for use with renewables [42]; the term “electrolyzer” hereafter refers specifically to this type.

A PEM electrolysis cell produces hydrogen (H_2) and oxygen (O_2) by splitting water using direct current. It consists of an anode, a cathode, and a solid polymer electrolyte membrane that conducts protons while

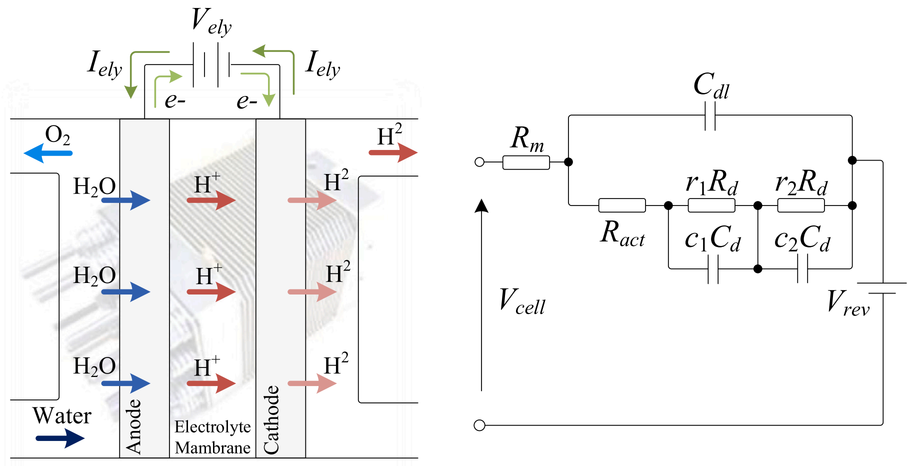

(a) (b)

Fig. 2. Schematic of a PEM electrolysis cell.

separating the electrodes. During operation, deionized water is fed to the anode, where it splits into protons, electrons, and oxygen gas. Protons pass through the membrane to the cathode, while electrons flow through an external circuit. At the cathode, protons and electrons recombine to form hydrogen gas. The overall reaction is:

$$\text{Anode: } H_2O \rightarrow \frac{1}{2}O_2 + 2H^+ + 2e^-, \quad \text{Cathode: } 2H^+ + 2e^- \rightarrow H_2,$$
$$\text{Overall: } H_2O \rightarrow H_2 + \frac{1}{2}O_2. \tag{5}$$

To start the above reaction, the supplied voltage for the electrolyzer cell must be sufficient to overcome the reversible voltage and different overpotentials. The relationship between the cell voltage and the current density is typically represented by the polarization curve, which can be formulated as [43,44]:

$$V_{cell} = V_{rev} + V_{act} + V_{ohm} + V_{conc}\ , \tag{6}$$

where V_{cell} is the cell voltage (the actual required dc voltage); V_{rev} denotes the reversible voltage (1.23 V under 25 °C and 1 atm); V_{act}, V_{ohm}, V_{conc} represent the activation, ohmic, and concentration overpotentials, respectively, and are detailed as:

$$\begin{cases} V_{act} = \frac{RT}{\alpha_a F}\text{arcsinh}\left(\frac{j}{2j_{0,a}}\right) + \frac{RT}{\alpha_c F}\text{arcsinh}\left(\frac{j}{2j_{0,c}}\right) \\ V_{ohm} = \frac{t_{mem}}{\sigma_{mem}A_{cell}}I_{cell} \\ V_{conc} = \frac{RT}{4F}\ln\left(\frac{C_{O2,mem}}{C_{O2,ch}}\right) + \frac{RT}{2F}\ln\left(\frac{C_{H2,mem}}{C_{H2,ch}}\right) \end{cases}. \tag{7}$$

In Eq. (7), R, T, and F are the gas constant, temperature, and Faraday's constant, respectively. α_a and α_c are the charge transfer coefficients, and j is the current density. $j_{0,a}$ and $j_{0,c}$ denote the exchange current densities at the anode and cathode. t_{mem} and σ_{mem} represent the membrane thickness and proton conductivity. A_{cell} is the cell's active area, and I_{cell} is the total current. $C_{O_2,mem}$, $C_{O_2,ch}$, $C_{H_2,mem}$, and $C_{H_2,ch}$ are the oxygen and hydrogen concentrations at the membrane and channel interfaces. These overpotentials arise from kinetics of the electronic charge transfer, mass transfer and ohmic losses in the electrolyte.

The electrolyzer characteristics expressed by (6) can be represented by an equivalent electrical circuit as shown in Fig. 2(b) [44,45], when focusing on power system dynamics studies. Here, R_m, R_{act}, and R_d are used to emulate the production of voltage drops relevant to the overpotentials of V_{ohm}, V_{act} and V_{conc}, respectively. C_{dl} and C_d represent the double-layer capacitance effect during the electrolysis reaction, which results from the accumulation of charge on both sides of the membrane along with the opposite type of charge present on the electrodes' surfaces. Moreover, r_1, r_2, c_1, c_2 are the scaling coefficients. The double-layer capacitance effect will cause a time delay in establishing the voltage when the current is input instantaneously. These parameters in the equivalent circuit can be estimated and fitted through experimental testing for electrolyzers.

Furthermore, the overall electrolyzer stack is modelled by connecting N_{cell} individual cells in series. The stack voltage V_{stack} and current I_{stack} can be obtained based on the cell voltage V_{cell} and current I_{cell}, as follows:

$$V_{stack} = N_{cell}V_{cell}, \quad I_{stack} = I_{cell}. \tag{8}$$

In addition, according to faraday's law, the hydrogen production flow in Nm^3/h can be calculated as:

$$\dot{n}_{H_2}^{in} = \frac{\eta_F N_{cell} I_{stack}}{zF} \cdot 22.4136 \cdot 3.6\ , \tag{9}$$

where z is the number of transferred electrons (equal to 2), and η_F is the faraday efficiency, assumed to be 1.

2.3. Design of multiphase interleaved buck converter

2.3.1. Current sharing and balance between phases

Each phase of the multiphase interleaved buck converter shares the total output current supplied to the electrolyzer, and in an N-phase interleaved structure, the n^{th} phase is shifted by:

$$\theta_n = 360^\circ \cdot \frac{n-1}{N} \quad (n = 1, 2, 3, \ldots, N). \tag{10}$$

For example, $\theta_1 = 0^\circ, \theta_2 = 90^\circ, \theta_3 = 180^\circ, \theta_4 = 270^\circ$ if $N = 4$. Moreover, equal current sharing is essential to minimize thermal stress, improve overall efficiency, and ensure reliable operation of the power converter system. The basic control algorithm of phase current sharing is described in Fig. 3. The average inductor current (RMS value) across all phases is used as the reference for each individual inductor current, and the deviation, processed by a PI controller, is added to the modulation waveform to achieve balanced current sharing:

$$D_{in,ref} = G_n \cdot \left(\sum_{n=1}^{N} \frac{I_{opn,\text{RMS}}}{N} - I_{opn,\text{RMS}}\right), \tag{11}$$

where $D_{in,ref}$ is the generated duty cycle in the current sharing loop, and G_n represents the overall gain (transfer function) of the PI controller assigned to phase n.

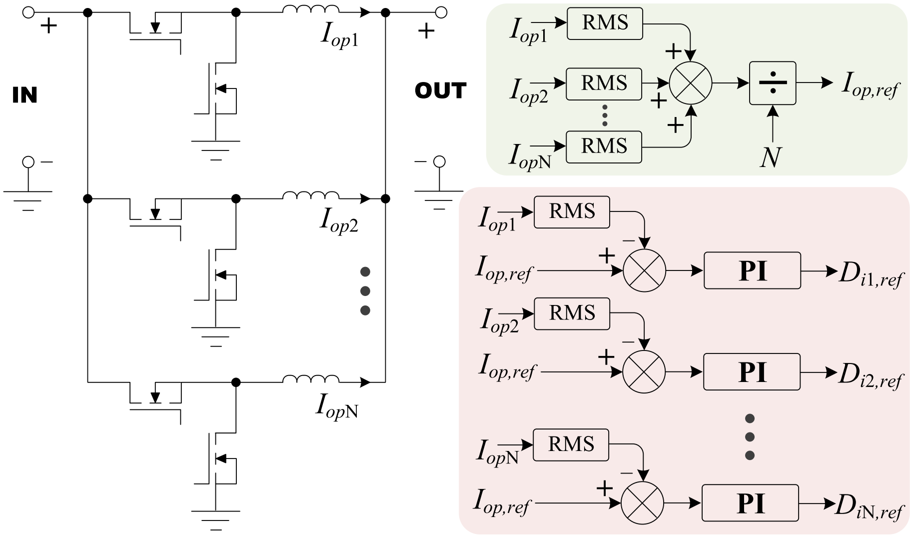

Fig. 3. Control algorithm of current balance between phases in the multiphase interleaved buck converter.

It should be noted that this current balance method is only applied in simulation, whereas a more practically applicable trial-and-error approach is used in the hardware to achieve current balance among phases. An incremental correction approach is adopted in the hardware based on current deviation, where the difference between each phase current and the average current ($\Delta I_{opn} = \sum_{n=1}^{N} I_{opn,\mathrm{RMS}}/N - I_{opn,\mathrm{RMS}}$) is used to dynamically update a correction value $\Delta D_{n,ref}$:

$$\Delta D_{n,ref}(k) = \Delta D_{n,ref}(k-1) + c \cdot \Delta I_{opn}(k), \tag{12}$$

where c is a current correction coefficient. This correction is then superimposed on the base duty cycle reference $D^{(0)}_{n,ref}$ in the main controller to fine-tune $D_{n,ref}$:

$$D_{n,ref}(k) = D^{(0)}_{n,ref}(k) + \Delta D_{n,ref}(k). \tag{13}$$

2.3.2. Harmonic elimination principle

To minimize the total output current ripple in an interleaved multiphase buck converter, the ripple currents of individual phases are analyzed in the frequency domain. Let $i_o(t)$ denote the total ripple current from the converter output, defined as the summation of the ripple components from all N parallel phases:

$$i_o(t) = \sum_{n=1}^{N} i_n(t), \tag{14}$$

where $i_n(t)$ is the ripple current of the n^{th} phase in the time domain. Each $i_n(t)$ can also be expanded into its Fourier series representation as:

$$i_n(t) = \sum_{h=1}^{\infty} A_{nh} \cos(h\omega t - h\theta_{0n} - \phi_{nh}), \tag{15}$$

where h refers to the harmonic order, A_{nh} is the amplitude of the h^{th} harmonic of the n^{th} phase, θ_{0n} is the initial phase shift angle of the n^{th} phase, ϕ_{nh} denotes the phase offset associated with the h^{th} harmonic of phase n. The amplitude A_{nh} depends on the duty cycle D_n, the ripple amplitude Δi_n, and the harmonic order h, expressed as:

$$A_{nh} = \left|b_{nh}\right|, \quad b_{nh} = \frac{-\Delta i_n (-1)^h}{h^2 D_n (1 - D_n)\pi^2} \sin\left[h(1 - D_n)\pi\right] \tag{16}$$

To suppress the h^{th} harmonic in the total ripple current, the phasor sum of all corresponding harmonic components (to rewrite Eq. (15) as a phasor $\sum_{n=1}^{N} A_{nh} e^{-j(h\theta_{0n} + \phi_{nh})}$) can be formulated as a minimization problem:

$$\min\left(\left| A_{1h} + \sum_{n=2}^{N} A_{nh} \cdot \cos(\phi_{nh}) + i \sum_{n=2}^{N} A_{nh} \cdot \sin(\phi_{nh}) \right|\right), \tag{17}$$

where $\phi_{1h} = 0$ is chosen so that the phasor of the first phase contributes only to the real part of the total vector sum. This minimization formulation captures the geometric condition for harmonic cancellation: if the harmonic phasors of all phases can be arranged to form a closed polygon in the complex plane, their vector sum will be zero, thereby eliminating the corresponding harmonic from the total output ripple. This leads directly to the following harmonic elimination criterion:

$$\sum_{n=1}^{N} A_{nh} e^{-j(h\theta_{0n} + \phi_{nh})} = 0, \tag{18}$$

which defines the necessary set of phase shifts θ_{0n} to achieve perfect cancellation of the h^{th} order ripple.

3. System-level control schemes

3.1. Steady-state operation

For the single-converter PVEC system configuration, the interleaved buck converter is limited to regulating a single electrical quantity (external loop control target) on the PV or electrolyzer side. It is expected to track the maximum power point on the PV side to ensure real-time solar energy utilization for hydrogen production. The control diagram of the single interleaved buck converter is shown in Fig. 4(a), using the P&O MPPT algorithm as:

$$D^{single}_{mppt,ref} = \left(V_{pv} - f(V_{pv}, I_{pv})\right) \cdot G^{single}_{mppt} \cdot G_{inner}, \tag{19}$$

where $D^{single}_{mppt,ref}$ is the duty cycle generated by the MPPT control loop in the single-converter; $f(V_{pv}, I_{pv}) = V_{pv,ref}$ is determined by the MPPT algorithm, G^{single}_{mppt} is the gain of the PI controller in the MPPT loop; G_{inner} represents the inner controller gain (with $G_{inner} = 1$ if the inner loop is not used).

For the double-converter PVEC system configuration, two control targets can be selected in the two interleaved buck converters [illustrated in Fig. 4(b) and (c)]. Moreover, two control schemes are available, including *i)* mode 1 - converter 1 tracks the PV maximum power $P_{pv,max}$,

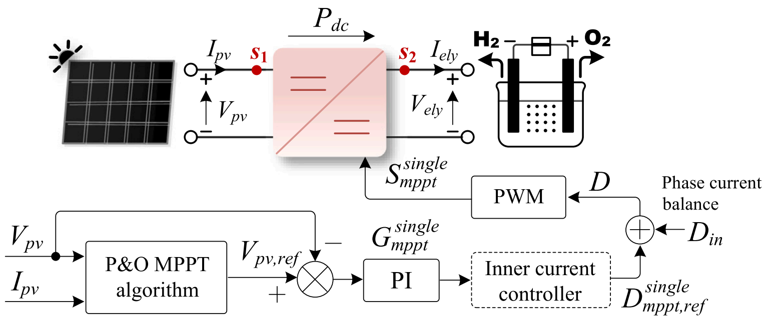

Single interleaved buck converter

(a)

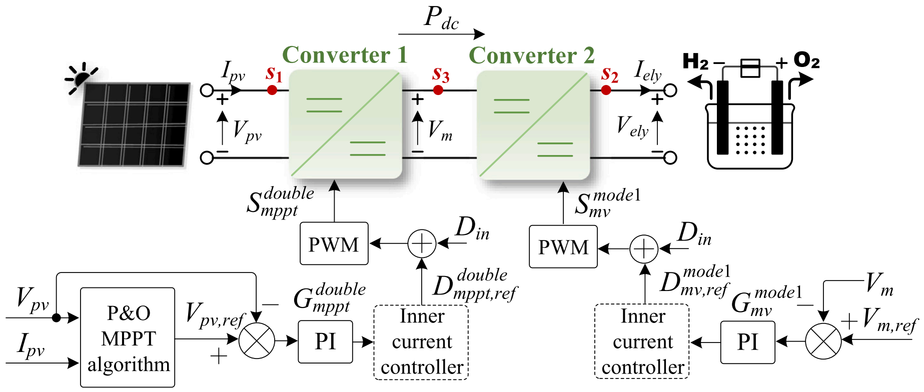

Dual interleaved buck converters using control mode 1

(b)

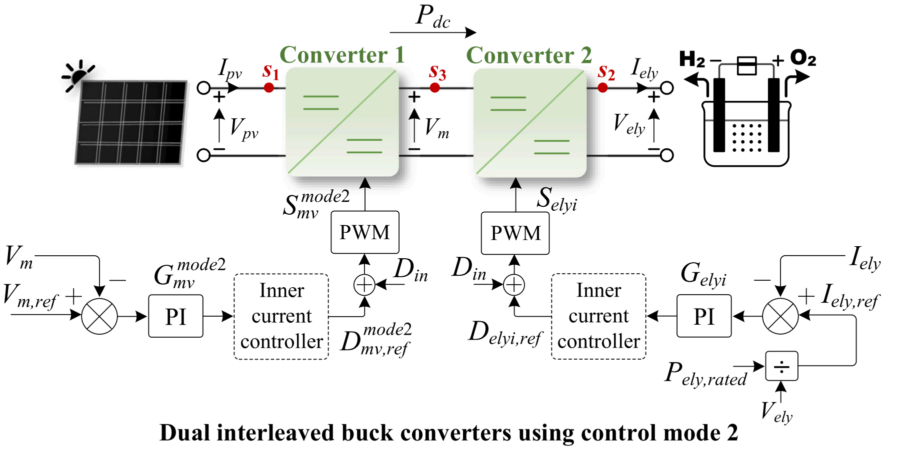

Dual interleaved buck converters using control mode 2

(c)

Fig. 4. Control diagrams of standalone PVEC systems using single and dual interleaved buck converters: (a) single interleaved buck converter, (b) dual interleaved buck converters using control mode 1, and (c) dual interleaved buck converters using control mode 2.

and converter 2 controls the middle dc-link voltage V_m; *ii*) mode 2 - converter 1 regulates the middle dc-link voltage V_m, and converter 2 determines the output current I_{ely} (electrolyzer input current). The two control modes can be expressed by:

$$\begin{cases} D_{mppt,ref}^{double} = \left(V_{pv} - f(V_{pv}, I_{pv})\right) \cdot G_{mppt}^{double} \cdot G_{inner} \\ D_{mv,ref}^{mode1} = \left(V_m - V_{m,ref}\right) \cdot G_{mv}^{mode1} \cdot G_{inner} \end{cases}, \quad \text{for control mode 1}, \tag{20}$$

$$\begin{cases} D_{mv,ref}^{mode2} = \left(V_m - V_{m,ref}\right) \cdot G_{mv}^{mode2} \cdot G_{inner} \\ D_{elyi,ref} = \left(I_{ely} - I_{ely,ref}\right) \cdot G_{elyi} \cdot G_{inner} \end{cases}, \quad \text{for control mode 2}, \tag{21}$$

where $D_{mppt,ref}^{double}$, $D_{mv,ref}^{mode1}$, $D_{mv,ref}^{mode2}$, $D_{elyi,ref}$ refer to the obtained duty cycles in the corresponding loops of MPPT control, middle dc-link voltage control and electrolyzer current control; G_{mppt}^{double}, G_{mv}^{mode1}, G_{mv}^{mode2}, G_{elyi} represent the corresponding gains of different PI controllers in the two control modes.

When the mode 1 control scheme is adopted, the electrolyzer input power follows the maximum power tracked from the PV, whereas the mode 2 scheme enables precise control of the electrolyzer input current at the cost of maximum PV utilization efficiency. It should be noted that the dc current reference is calculated by dividing the electrolyzer power rating by the real-time electrolyzer voltage, as depicted in Fig. 4(c).

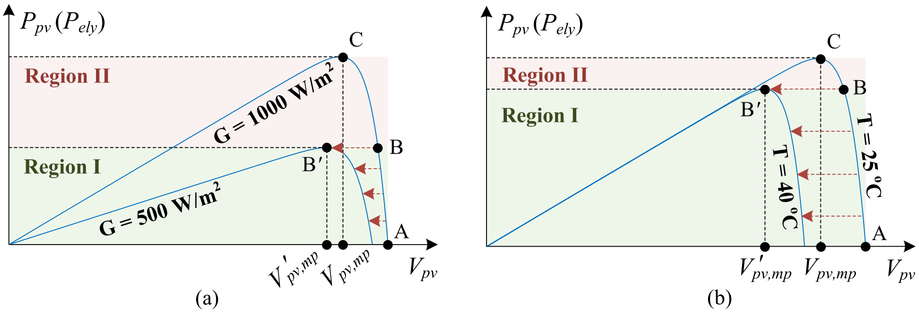

Fig. 5. Impact of solar irradiance reduction and cell temperature increase under control mode 2 in the dual-converter PVEC system: (a) solar irradiance reduction, and (b) cell temperature increase.

3.2. Low power ride-through (LPRT) strategies

When solar irradiance is reduced (e.g. due to passing clouds or diurnal variations) and/or the cell temperature increases (e.g. under prolonged sun exposure or poor ventilation), the PV array experiences a reduction in output power, primarily due to decreased current from lower irradiance and reduced voltage resulting from higher temperature. Since the maximum PV power is tracked in the single-converter PVEC system, the electrolyzer power input naturally decreases with the reduction in solar irradiance. Similar to the single-converter system, the dual-converter system operating under control mode 1 can also ensure that the electrolyzer power output follows changes in solar irradiance. Meanwhile, the middle dc-link voltage reference does not need to be adjusted, as the voltage at the maximum power point $V_{pv,mp}$ remains relatively stable.

However, as shown in Fig. 5 (ignoring power losses), if control mode 2 is adopted in the dual-converter PVEC system, the fixed input dc current control of the electrolyzer [Fig. 4(c)] could lead to a power mismatch when the PV maximum power (point B') is lower than the regulated electrolyzer power (initially in Region II), further leading to system collapse. Therefore, two LPRT strategies are presented to achieve power matching between the PV output and the electrolyzer input for control mode 2 under significant solar irradiance reduction.

In the first LPRT strategy (LPRT strategy I), as shown in Fig. 6(a), the dc current reference $I_{ely,ref}$ is forcibly decreased when the middle dc-link voltage is detected to fall below κV_{dcm}, where κ lies within (0.9, 1). The dc current reference is updated by the current reachable PV maximum power $P_{mp}(G,T)$:

$$P_{mp}(G,T) = P_{mp,ref} \cdot \frac{G}{G_{ref}} \cdot [1 + \beta(T - T_{ref})] \tag{22}$$

obtained from

$$\begin{aligned} P_{mp}(G) &= V_{mp,ref}(G) \cdot I_{mp,ref}(G) \approx V_{mp,ref} \cdot I_{mp,ref} \cdot \frac{G}{G_{ref}} \\ &= P_{mp,ref} \cdot \frac{G}{G_{ref}}, \text{ and} \end{aligned} \tag{23}$$

$$P_{mp}(T) = P_{mp,ref} + \beta \cdot P_{mp,ref} \cdot (T - T_{ref}), \tag{24}$$

where β refers to the temperature coefficient of the maximum power (%/°C). Considering the power losses, a user-defined loss coefficient ρ is introduced, and accordingly, the actual power supplied to the electrolyzer for updating the current reference is given by:

$$P_{ely} = (1 - \rho) \cdot P_{mp}(G,T). \tag{25}$$

Moreover, an S-R flip-flop circuit [46] is employed to prevent false triggering caused by low dc-link voltage during system start-up or recovery phases following transient disturbances. The operating principle of the flip-flop is depicted in Fig. 6 as well. Specifically, the “enable” signal connected to the “R” (reset) terminal serves as a control input to activate or deactivate the LPRT strategy. When the enable signal is set to 1, the LPRT function is disabled.

In addition to LPRT strategy I, it is also practical to switch from control mode 2 to control mode 1, with converter 1 used to track the current PV maximum power (LPRT strategy II). As shown in Fig. 6(b), the duty cycles ($D^{double}_{mppt,ref}$, $D^{mode1}_{mv,ref}$) generated in the control mode 1 are used for subsequent PWM signal generation, and all integrators within the switched control loops are accordingly reset. Consistent with LPRT strategy I, the transition between modes is initiated when the middle dc-link voltage drops below κV_{dcm}, and the S-R flip-flop is likewise applied to suppress unwanted switching during the system start-up. It is worth mentioning that the PV array is able to supply the required power to the electrolyzer under control mode 2 if its initial operating point lies in Region I (Fig. 5), where the PV has not yet reached its maximum power. Table 4 summarizes the available control methods and the LPRT capabilities for standalone PVEC systems with single and dual interleaved buck converters.

4. Simulation results

Two 5 kW standalone PVEC systems are established in Simulink, using a single interleaved buck converter and dual interleaved buck converters, respectively. The detailed parameters of the PV, PEM electrolyzer and interleaved buck converters are provided in Table 5. Ten GoodWe BMT-P2/132 A 525 W PV modules [47], arranged in two parallel strings with five modules per string, are used to deliver a maximum power output of 5.25 kW. The electrolyzer system is constructed based on the cell design developed in [45]. Utilizing a bipolar configuration, 11 cells are connected in series to scale up the system to a 5 kW capacity. The system parameters are correspondingly scaled based on the RC circuit-based cell model parameters provided in [45]. The 5 kW rating is selected as a representative level to capture key system characteristics under realistic operating conditions. Scaling to higher power mainly affects voltage and current levels, without fundamentally changing system behavior.

Since this paper focuses on system-level control for both single- and dual-converter configurations, only line losses are considered in the simulation, where a loss of 250 W under full power operation corresponds to an equivalent resistance of 0.004 Ω between the converter and the electrolyzer (approximately 5%). The complete loss assessment will be presented in the experimental results (Section 5).

In the single-converter configuration, MPPT control based on the P&O algorithm is implemented with a perturbation step size of $\delta = 0.2$ and a power variation threshold of $\varepsilon = 0.05$. The same parameter settings are adopted for converter 1 operating in control mode 1 of the dual-converter configuration. For control mode 2 in the dual-converter configuration, the middle dc-link voltage drop threshold is set to 1.2 V ($\kappa = 0.98$) to determine the control mode transition. In addition, the user-defined loss coefficient ρ is set to 0.15 (5% full power

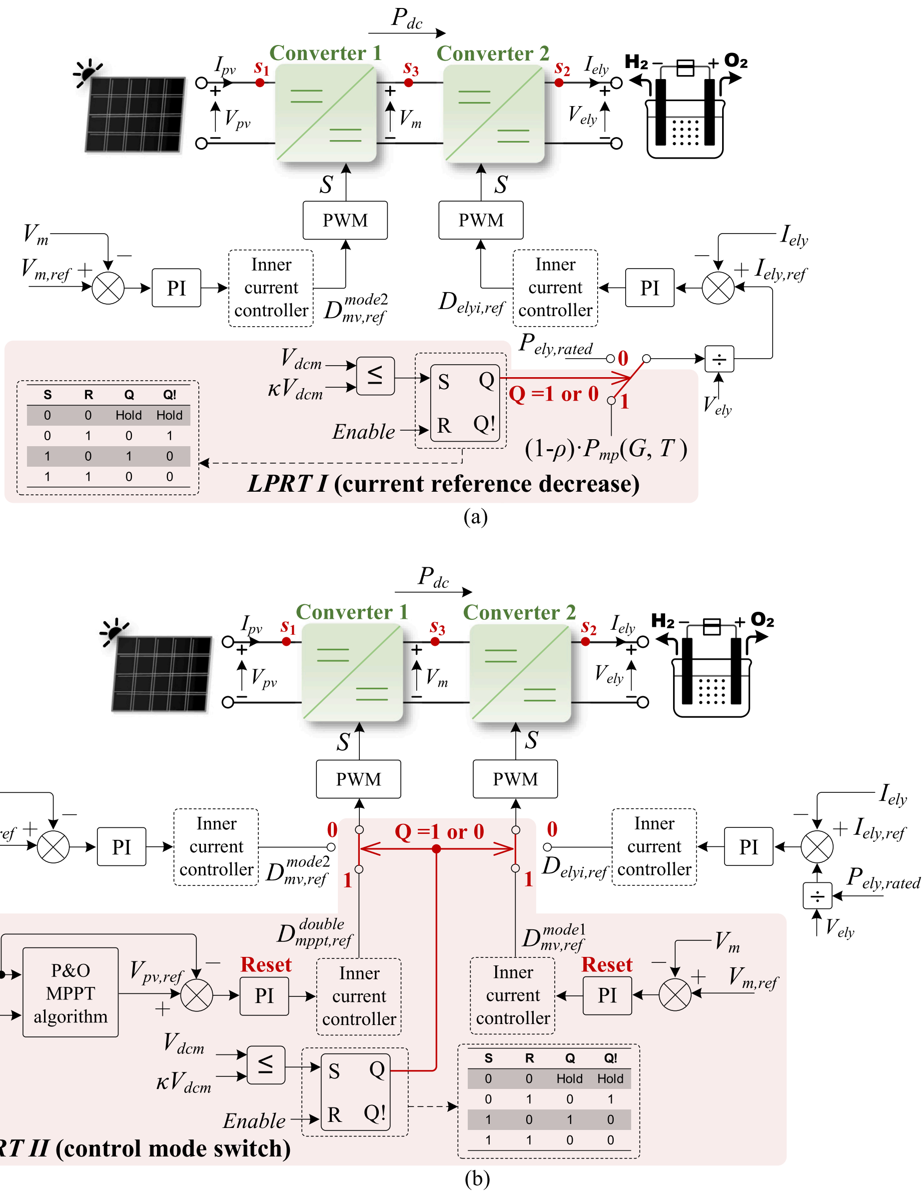

(a)

(b)

Fig. 6. LPRT control diagrams of standalone PVEC systems using dual interleaved buck converters under control mode 2: (a) LPRT I - electrolyzer current reference change, and (b) LPRT II - control mode switch.

Table 4
Control methods for standalone PV-electrolyzer systems using single and dual dc/dc converters.

Single-converter	Control: PV P_{mp}	LPRT: ✓✓
Dual-converter	Control mode 1: PV P_{mp}; middle dc-link V_m Control mode 2: middle dc-link V_m; electrolyzer I_{ely}	LPRT: ✓✓ LPRT: ✓

✓✓: natural LPRT; ✓: LPRT using the two proposed strategies.

loss and an additional 10% for safety margin and transient performance) for control mode 2, to ensure reliable LPRT following a significant PV power reduction, where the electrolyzer power is updated to $P_{ely} = 0.85P_{mp}(G, T)$ (25) to revise the dc current reference.

4.1. Standalone PVEC system using single-converter configuration

4.1.1. Solar irradiance reduction

As shown in Fig. 7(a), the PV system initially operates at the maximum power point with an output power of 5.25 kW, a voltage of 205.1 V, and a current of 25.6 A. At 1 s, the solar irradiance decreases from 1000 W/m^2 to 800 W/m^2, and then further drops to 400 W/m^2 at 1.2 s. Since the MPPT algorithm is implemented in the interleaved buck converter, the PV system continuously operates at its maximum power point, with 4.2 kW for G = 800 W/m^2 and 2.1 kW for G = 400 W/m^2. The power input to the PEM electrolyzer closely tracks the real-time maximum power from the PV system, with 5 kW (20 V, 250 A) for G = 1000 W/m^2, 4.02 kW (19 V, 211.6 A) for G = 800 W/m^2 and 2.04 kW (16.7 V, 122.3 A) for G = 400 W/m^2, based on the power flow analysis [48]. As the input power decreases, hydrogen production also declines, for instance, from approximately 1.15 Nm^3/h at 5 kW to 0.97 Nm^3/h at 4.02 kW, and further reducing to 0.56 Nm^3/h at 2.04 kW. Meanwhile, the electrolyzer system efficiency increases with the reduction in input power, rising from 81.42% at 5 kW to 85.42% at 4.02 kW, and reaching 97.18% at 2.04 kW. This trend is primarily attributed to reduced ohmic and activation overpotentials at lower current densities, cutting down the energy losses within the stack.

Fig. 7 also illustrates the inductor currents in each phase, where the phases are sequentially shifted by 90°. By applying the current

Table 5
Parameters of PV and electrolyzer in simulation.

PV parameters (525 W in each module [47]) Irradiance = 1000 W/m^2, T = 25°C	
Maximum power P_{mp}	5250 W
Parallel strings, modules per string	2, 5
MPPT voltage V_{mp}	205.1 V
Open-circuit voltage V_{oc}	238.9 V
MPPT current I_{mp}	25.6 A
Short-circuit current I_{sc}	27.0 A
P_{mp} temperature coefficient β	-0.35%/°C
Electrolyzer parameters [45]	
Rated power $P_{ely,rated}$	5000 W
Number of cells N_{cell}	11
Reversible voltage V_{rev}	13.519 V
Fitted resistance R_m, R_{act}, R_d	0.0103 Ω, 0.00651 Ω, 0.0093 Ω
Fitted coefficient r_1 r_2	0.097, 0.888
Equivalent steady-state resistance R_{eq}	0.0259 Ω
Fitted capacitance C_{dl}, C_d	1.394 F, 47.522 F
Fitted coefficient c_1, c_1	0.027, 0.36
Converter parameters	
Power rating	5000 W
Inductor	0.9 mH
Input capacitor	0.5 mF
Output capacitor (single conv.)	1 mF
Output capacitor (dual conv.)	1 mF
Middle capacitor (dual conv.)	3 mF
Switching frequency	20 kHz
Middle dc-link voltage reference $V_{m,ref}$	60 V
Electrolyzer current referenc* $I_{ely,ref}$	250 A

* $I_{ely,ref}$ is obtained from $P_{ely,rated}/V_{ely}$.

balancing strategy described in Section 2.3.1, the currents in all four phases are evenly distributed (average 62.5 A) to collectively supply the total current (250 A) required by the electrolyzer. The output current ripple (prior to filtering) of the converter is also reduced through the summation of all phase currents, as theoretically explained in Section 2.3.2.

4.1.2. PV cell temperature increase

An increase in cell temperature can also result in a reduction of PV power output. Fig. 7(b) shows the impact of cell temperature on the standalone single-converter PVEC system, where the temperature is raised from 25 °C to 40 °C at 1 s. In addition, the solar irradiance is decreased from 1000 W/m^2 to 800 W/m^2 at 1.2 s to show the co-influence of cell temperature increase and solar irradiance reduction. An increase in temperature from 25 °C to 40 °C results in a reduction of the PV maximum power from 5 kW to 4.9744 kW, as determined by (24). The electrolyzer power is correspondingly decreased to 4.74 kW (19.75 V, 240.2 A) in steady state. Following the irradiance reduction to 800 W/m^2, the PV maximum power further decreases to 3.9795 kW. Consequently, the power delivered to the electrolyzer is 3.81 kW, with a voltage of 18.8 V and a current of 203.1 A. As a result of the reduced power supply to the electrolyzer, hydrogen production correspondingly declines, from approximately 1.15 Nm^3/h at 5 kW to 1.10 Nm^3/h at 4.74 kW, and further to 0.93 Nm^3/h at 3.81 kW. In contrast, the system exhibits improved efficiency under lower power input conditions, increasing from 81.42% at 5 kW to 82.08% at 4.74 kW, and reaching 86.32% at 3.81 kW.

4.2. Standalone PVEC system using dual-converter configuration

4.2.1. Solar irradiance reduction & PV cell temperature increase – control mode 1

In the dual-converter setup, real-time PV MPPT is realized by assigning MPPT control to converter 1 and dc-link voltage regulation (60 V) to converter 2. Fig. 8(a) and (b) depict the system response to a reduction in solar irradiance from 1000 W/m^2 to 800 W/m^2 and 400 W/m^2, and to a cell temperature increase from 25 °C to 40 °C, respectively, with an additional irradiance drop applied at 1.2 s in the latter case. The power, voltage, and current changes in the electrolyzer are identical to those in the single-converter configuration, as converter losses are neglected in the simulation, while the differences will be revealed in the experimental results.

During all system disturbances, the middle dc-link voltage V_{dcm} remains well-regulated at 60 V, without significant transient deviations. Due to the presence of a middle dc-link capacitor in this dual-converter configuration, the transient response of the electrolyzer is slower compared to the single-converter configuration. This slower dynamic behavior results from two factors: the transient associated with dc-link voltage regulation and the slow voltage response caused by the electrolyzer's effective double-capacitance effect.

4.2.2. Solar irradiance reduction & PV cell temperature increase – control mode 2

When control mode 2 (converter 1 - middle dc-link voltage V_m, converter 2 - electrolyzer current I_{ely}) is adopted in the dual-converter configuration, a power mismatch may arise under PV power reduction due to irradiance reduction and temperature increase. As described in Section 3.2, two LPRT strategies (current reference decrease and control mode switch) can be used to ensure safe system operation.

LPRT Strategy I (Current reference decrease):. Both the full power start-up (5 kW electrolyzer power, Fig. 9) and non-full power start-up (3 kW electrolyzer power, Fig. 10) are examined under control mode 2 and LPRT Strategy I. For the full power start-up scenario, the effects of irradiance reduction [1000 W/m^2 to 500 W/m^2, Fig. 9(a)] and the temperature increase [25 °C to 40 °C, Fig. 9(b)] are tested separately. At 1 s, the PV power reduction induced by either irradiance drop or temperature rise results in a sudden power mismatch, where the PV system cannot supply the required 5 kW for the electrolyzer. Consequently, the electrolyzer current reference is forced to decrease upon detection of the dc-link voltage drop (from 60 V to 58.8 V). Specifically, the electrolyzer power is reduced to 2231.85 W and 4228.24 W [$P_{ely} = 0.85P_{mp}(G, T)$ (25)], with the resulting current references being 132 A and 220 A, respectively. Accordingly, as the power decreases in both cases, the hydrogen production is reduced to 0.61 Nm^3/h and 1.01 Nm^3/h, respectively. Meanwhile, the electrolyzer system efficiency increases to 96.75% and 84.56%.

Unlike the full power start-up case, the system under non-full power start-up remains stable without the need for the LPRT strategy during the period from 1 s to 1.2 s (Fig. 10), following either a 200 W/m^2 irradiance reduction or a 15 °C temperature increase, when the electrolyzer initially operates at 3 kW (Region I in Fig. 5). However, a further irradiance reduction to 500 W/m^2 results in a power mismatch, requiring the electrolyzer power to be reduced to 2231.85 W (132 A) and 2114.12 W (126 A) under LPRT Strategy I. As a result, the hydrogen production decreases to 0.61 Nm^3/h and 0.58 Nm^3/h, respectively, while the electrolyzer system efficiency increases to 96.75% and 97.12%, respectively.

LPRT Strategy II (Control mode switch):. Figs. 11 and 12 illustrate the performance of the dual-converter system operating under control mode 2 with LPRT Strategy II, for the full power start-up scenario (5 kW electrolyzer power) and non-full power start-up scenario (3 kW electrolyzer power), respectively. In the full power start-up scenario, a direct irradiance reduction [1000 W/m^2 to 500 W/m^2, Fig. 11(a)] or a temperature increase [25 °C to 40 °C, Fig. 11(b)] leads to a power mismatch between the PV and the electrolyzer. This mismatch results in a remarkable drop in the middle dc-link voltage. Once this condition is detected, the control mode is switched from control mode II to control mode I, in which converter 1 adopts PV MPPT control. Hence, the electrolyzer power input tracks the real-time PV maximum power (stabilizing at

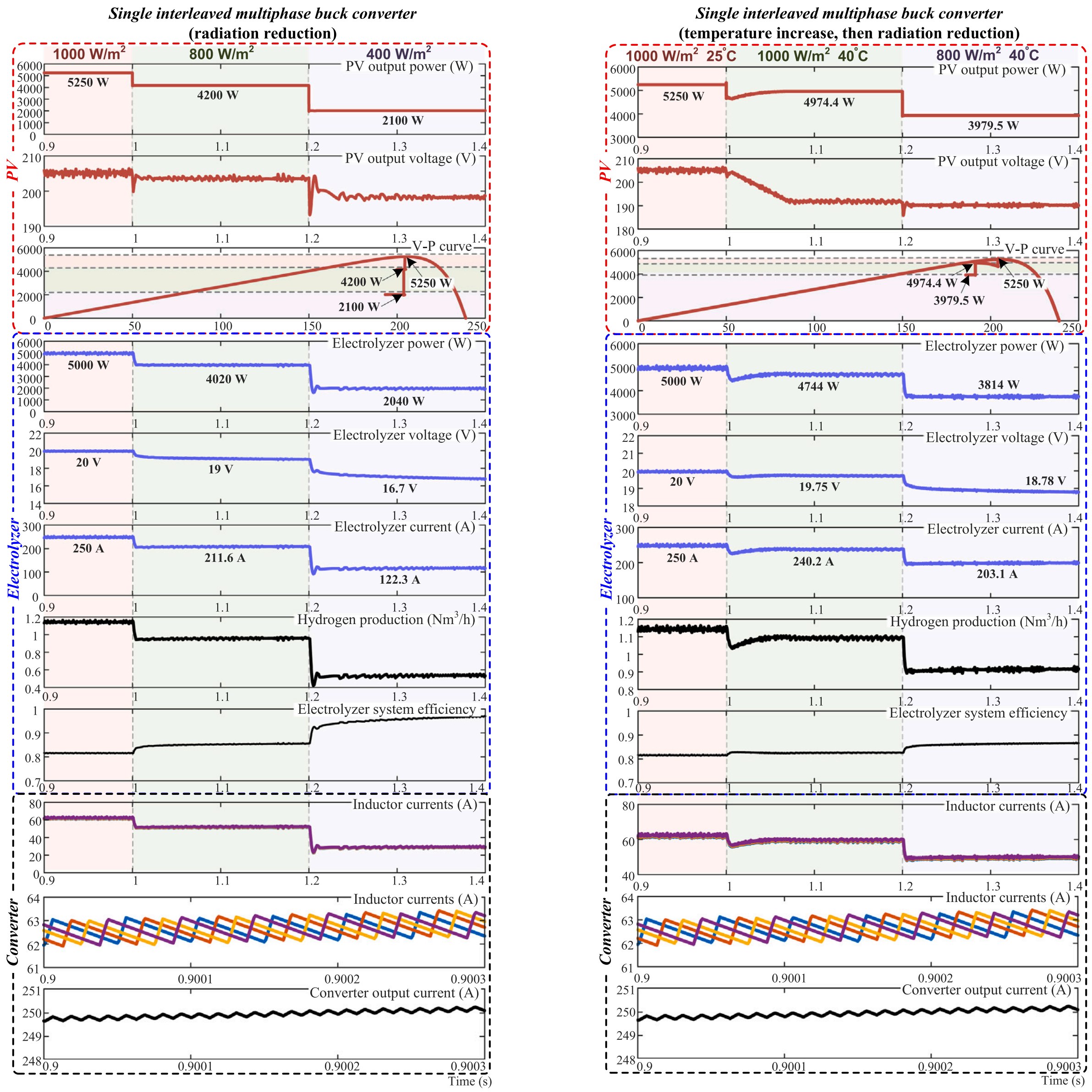

(a)

(b)

Fig. 7. Simulation results of the standalone PVEC system with single-converter configuration under various disturbance scenarios.

2625 W for PV under irradiance of 500 W/m^2 and temperature of 25 °C, and at 4974.4 W under irradiance of 1000 W/m^2 and temperature of 40 °C) after a short transient recovery stage (in less than 0.5 s). In both cases, as the electrolyzer power follows the decrease in PV power after switching to mode I, the hydrogen production correspondingly declines, while the system efficiency increases.

When the electrolyzer starts from 3 kW, a power mismatch also occurs at 1.2 s under two PV conditions: 500 W/m^2, 25 °C [Fig. 12(a)] and 500 W/m^2, 40 °C [Fig. 12(b)]. LPRT Strategy II is therefore triggered to initiate the control mode switch, allowing the system to effectively track the current PV maximum power, which reaches 2625 W and 2487.2 W in the two cases, respectively. Similarly, the hydrogen production decreases while system efficiency increases, as the electrolyzer power decreases in response to tracking the drop in PV power.

5. Experiment results

Experimental tests are conducted on a 200 W scaled-down PVEC system to validate the proposed schemes. The test platform is shown in Fig. 13(a). Both the single and dual interleaved multiphase buck converters employ GaN FETs, operating at a switching frequency of 200 kHz. In the single-converter configuration, MPPT control is implemented, while the dual-converter configuration operates either with MPPT and middle dc-link voltage (V_m) control, or with V_m control combined with electrolyzer current (I_{ely}) control. The PV and electrolyzer parameters are listed in Table 6, and the converter parameters are summarized in Table 7. An IT-N2121 solar emulator is used to replicate the output of a 220 W PV panel, while the electrolyzer is emulated by an IT-8513C+ programmable electronic load configured in constant-voltage (CV) mode at 6 V. This configuration reflects the intrinsic electrical characteristics of the electrolyzer, whose very low internal resistance (0.0324 Ω,

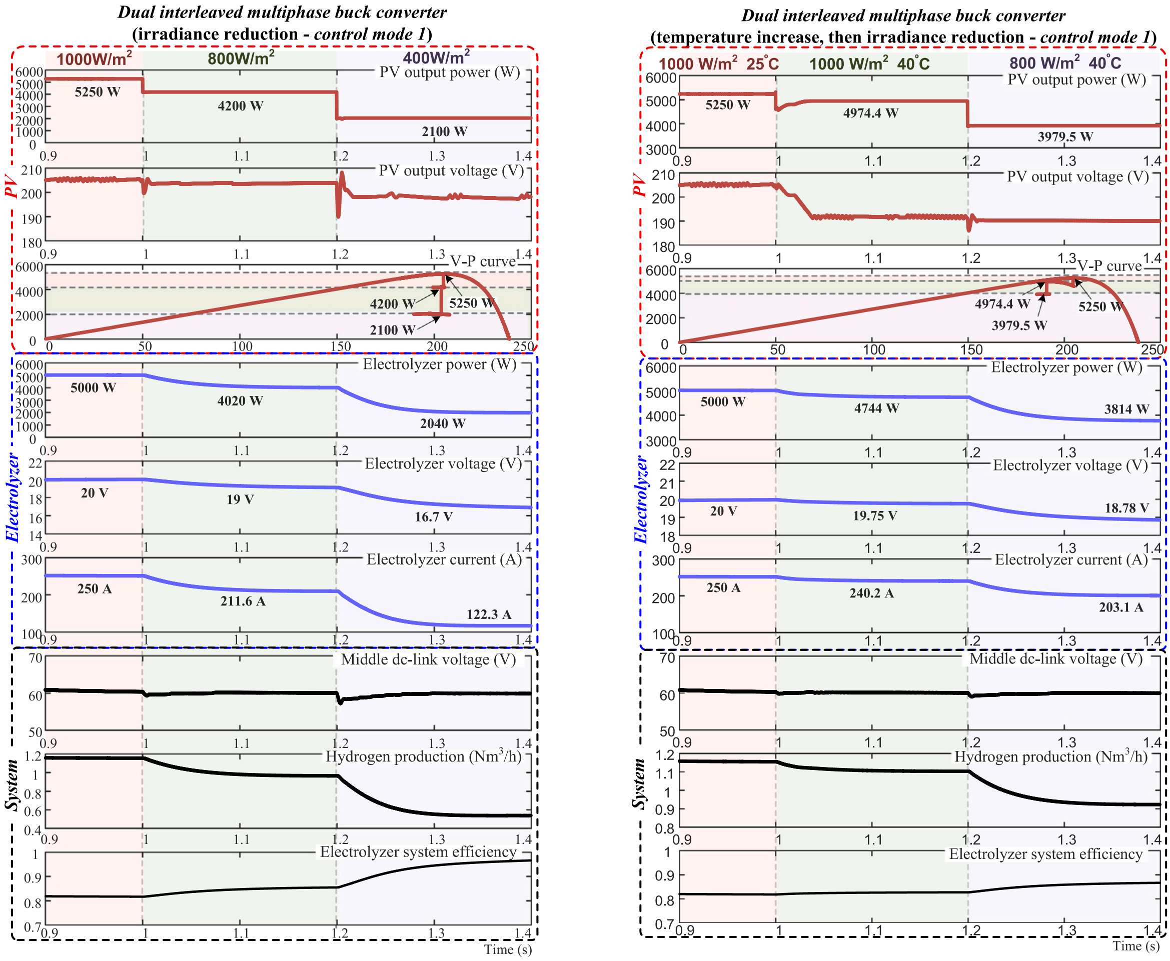

(a) (b)

Fig. 8. Simulation results of the standalone PVEC system with dual-converter configuration (control mode 1) under different disturbance scenarios.

calculated from the parameters in Table 6) ensures that its operating voltage remains nearly constant (4.92-6 V) across all current conditions. Since the electrolyzer voltage is almost fixed while its current and power vary significantly, the CV load provides a precise and effective equivalence for this study.

As shown in Fig. 13(b), two interleaved multiphase buck converters are constructed. Converter 1 is used alone in the single-converter configuration, whereas both Converter 1 and Converter 2 are connected in series for the dual-converter configuration. Although four phases are reserved in the hardware design, only two are activated, as the electrolyzer rated current of 33.3 A (200 W at 6 V) can be adequately supported by two phases. Each converter is controlled by an STM32F334C8Tx microcontroller, and every phase employs two GaN FETs (ISG3202), enabling compact operation at 200 kHz with a compact 10 cm × 10 cm PCB board. The ISG3202 (the production version of the ISG3201) is a 100 V GaN integrated half bridge power device designed for high frequency and high efficiency power conversion. It features a typical on resistance of approximately 2.4 mΩ, which helps reduce conduction losses in high current applications. The device exhibits a low total gate charge of around 9.2 nC, enabling fast switching transitions and reduced switching losses. In addition, the parasitic capacitances are relatively small, with typical values of (C_{iss} ≈ 1000 pF and C_{oss} ≈ 460 pF, which further supports high frequency operation. From a thermal perspective, the device has a junction to case thermal resistance of about 7.7 °C/W through the bottom thermal path, allowing efficient heat dissipation through the PCB. Combined with an operating junction temperature of up to 150 °C, these characteristics make the ISG3202 suitable for compact and high power density dc/dc converter applications.

5.1. Standalone PVEC system with single-converter configuration

Through MPPT control of the interleaved multiphase buck converter in the single-converter configuration, the electrolyzer load operates in a source-following mode, dynamically tracking the PV maximum power output (Fig. 14). A P&O-based MPPT algorithm is embedded in the STM32 microcontroller, with a perturbation step size of $\delta = 0.2$ and a power variation threshold of $\varepsilon = 0.01$. The instantaneous PV power reduction is also tested by emulating half solar irradiance, where the PV maximum power is reduced to 110 W and the MPPT voltage is 19 V. The results demonstrate, as shown in Fig. 14(a) and (b), that the designed converter can promptly track the PV maximum power following the significant PV power reduction.

Moreover, the output current is equally shared between the two phases by correcting the duty cycle in each phase, using Eqs. (12) and (13) in Section 2.3.1, as shown in Fig. 14(c) and (d). The inductor currents of the two arms also help reduce the ripple in the converter output current prior to filtering, which is further smoothed by the output capacitor (LC low-pass filter). In addition to equal phase current sharing, the designed multiphase interleaved buck converter delivers high

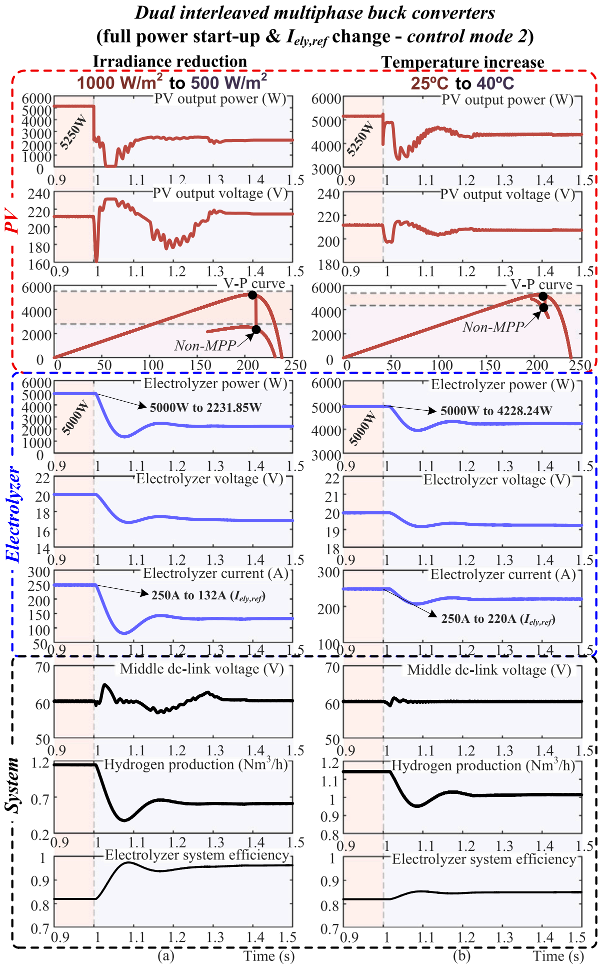

Fig. 9. Simulation results of the standalone PVEC system with dual-converter under control mode 2 and LPRT Strategy I (full power start-up).

power conversion efficiency, up to 98.6% under steady-state 220 W PV operation, and increasing to 99.0% under half irradiance conditions. Although the overall system efficiency from the PV terminal to the electrolyzer input is approximately 90.5% at 220 W PV power output, this includes around 21 W of total losses, with 17 W attributed to line losses.

5.2. Standalone PVEC system with dual-converter configuration

5.2.1. System performance under control mode 1

Under control mode 1, converter 1 still tracks the PV maximum power using the P&O MPPT algorithm, while converter 2 regulates the middle dc-link voltage at 12 V. This provides a two-stage voltage step-down, increasing the duty cycle from 0.3 in the single-converter configuration to 0.6 in the first stage and 0.5 in the second stage. The experimental test (200 W steady-state operation) shows the total power losses are around 28 W, including the 23 W power losses in lines and 5 W losses in converters (1.7 W in converter 1 with 99.1% efficiency and 3.3 W in converter 2 with 98.4% efficiency). These combined losses are inherently higher than a single-converter design due to the power dissipation by the second converter stage, yet this two-stage structure offers key advantages such as voltage decoupling, increased duty cycle range, and easier system scalability.

Fig. 15 demonstrates the experimental results under 220 W and 110 W maximum PV output, showing that converter 1 can rapidly track the PV maximum power as it decreases from 220 W to 110 W (V_{mp} = 19 V) [Fig. 15(a)], while converter 2 consistently maintains the intermediate dc-link voltage. Moreover, the phase arm currents are shared equally within each converter, as depicted in Fig. 15(c) and (d).

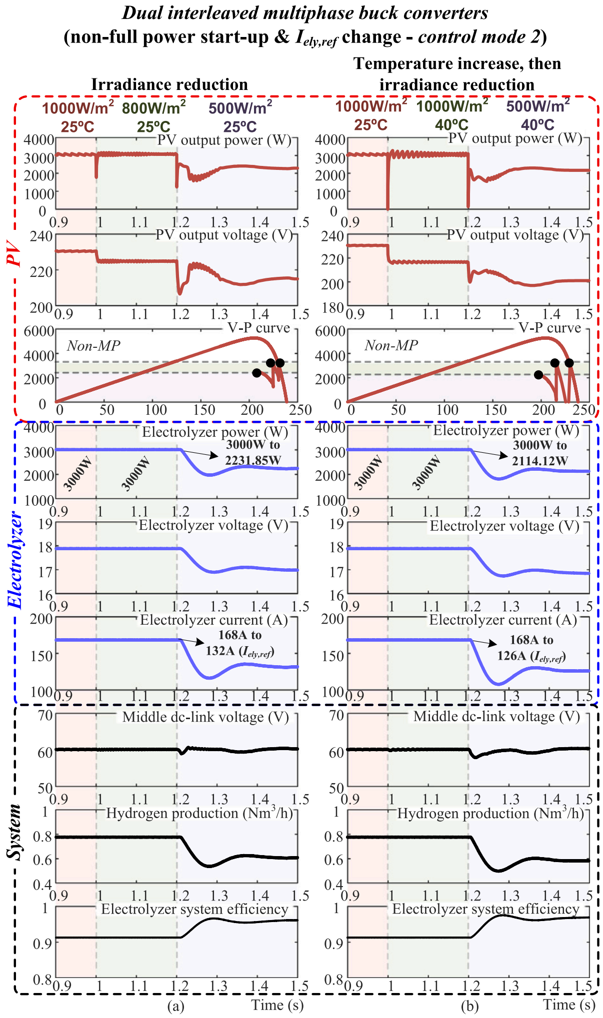

Fig. 10. Simulation results of standalone PVEC system with dual-converter under control mode 2 and LPRT Strategy I (non-full power start-up).

5.2.2. System performance under control mode 2

Unlike the dual-converter configuration under control mode 1, control mode 2 requires communication when there is a significant drop in the available maximum PV power, in order to reduce the electrolyzer current reference (LPRT I) or switch the control mode back to mode 1 (LPRT II). The two communication ports of the two boards are connected, as shown in Fig. 13(b). When the LPRT I control method (control logic in Fig. 6(a) and results in Fig. 16) is applied, and a low middle dc-link voltage level (11.5 V) is detected, the first converter takes over regulation of the dc-link voltage. Simultaneously, it sends a low-voltage signal to the second converter, prompting it to reduce the electrolyzer power P_{ely} to 93.5 W (based on a loss coefficient of 0.15 in (25)). This adjustment allows the reference current to be reduced to approximately 15.4 A, given that the output voltage of converter 2 is currently 6.08 V. Under the LPRT II scheme (control logic in Fig. 6(b) and results in Fig. 17), when a low middle dc-link voltage level is detected, the first converter switches to MPPT control, while the second converter transitions to regulating the middle dc-link voltage.

The implementation of both LPRT strategies offers smooth system recovery with minimal oscillation during current reference variation and control mode transitions, despite the PV power falling to zero

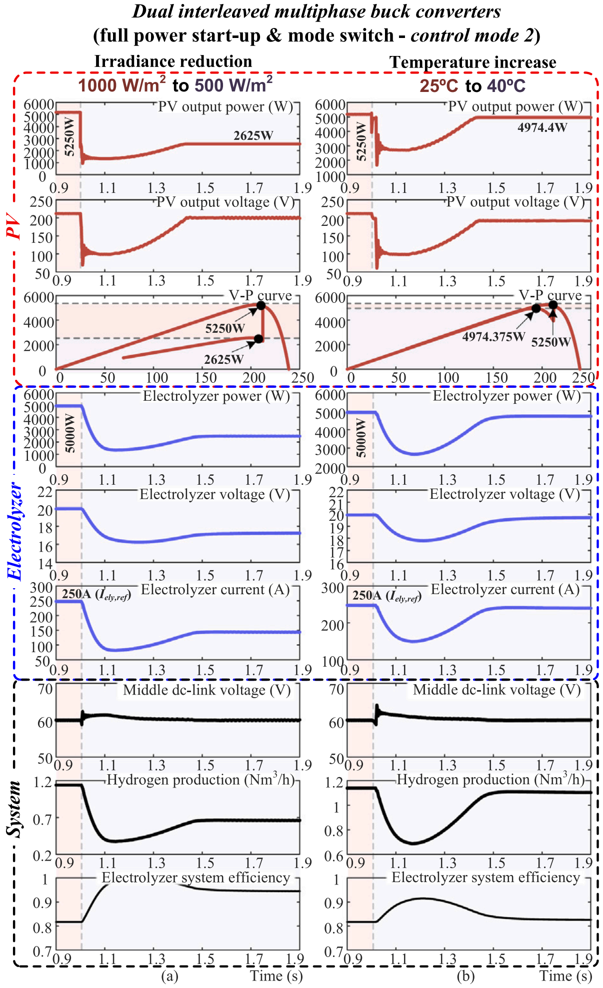

Fig. 11. Simulation results of a standalone PVEC system with a dual-converter under control mode 2 and LPRT Strategy II (full power start-up).

due to a sudden and significant solar irradiance drop. LPRT I necessitates precise, continuous tuning of the electrolyzer current reference according to solar variations. LPRT II, however, is designed to engage only after a major drop in PV power, where the system reverts to standard MPPT, thus offering a more straightforward implementation pathway.

5.3. Comparative analysis between simulation and experiment

The simulation and experimental results show good agreement in the normalized control behavior. In simulation, the 5 kW single stage case tracks the PV maximum power from 5.25 kW to 4.2 kW and 2.1 kW, while the electrolyzer power follows from 5.0 kW to 4.02 kW and 2.04 kW. In the 200 W experiment, the scaled prototype shows the expected performance, with the PV power decreasing from 220 W to 110 W. Under dual-stage control mode 1, converter 2 output decreases from 199.6 W to 101.9 W while the DC link remains close to 12.0 V. For control mode 2, LPRT is triggered, corresponding to a current reference of about 15.4 A. Although higher power losses are measured on the prototype, namely about 21 W in the single stage case and about 28 W in the dual-stage case, the converters efficiency remains high. At high switching frequencies, GaN devices exhibit increased conduction and switching losses. In addition, parasitic elements, dead-time effects, and digital sampling and control delays contribute significantly to the discrepancy between simulation and experimental results.

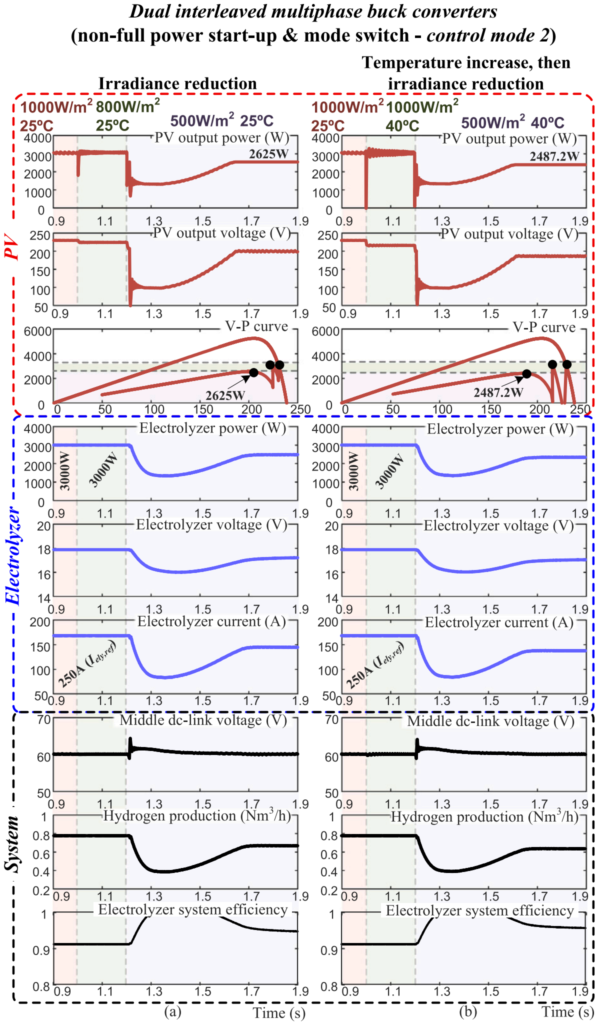

Fig. 12. Simulation results of a standalone PVEC system with a dual-converter under control mode 2 and LPRT Strategy II (non-full power start-up).

6. Discussion

6.1. Potential improvements

The single-stage converter offers a simple design with fewer components and potentially higher efficiency due to the absence of an intermediate stage, making it attractive for small-scale PVEC systems where cost and reliability are priorities. However, its single degree of freedom limits control, forcing the electrolyzer to follow the PV maximum power point. At higher power levels, the wide voltage mismatch can increase current stress and reduce operational flexibility. Future improvements for single-stage systems may include the adoption of isolated dc/dc converter topologies, which can provide flexible voltage matching, galvanic isolation, and improved fault protection.

The dual-stage architecture provides significantly enhanced control flexibility by introducing an intermediate dc-link, enabling independent regulation of the PV-side operating point and the electrolyzer current. This decoupling allows the electrolyzer to operate under controlled current conditions, facilitating more stable hydrogen production and improved system controllability. However, the additional conversion stage inevitably introduces increased system complexity, a higher component count, and additional power losses. A practical consideration for future research is the integration of energy storage at the intermediate dc-link in the dual-stage configuration. As identified in this study, the dc-link naturally serves as an effective interface for hybrid energy storage

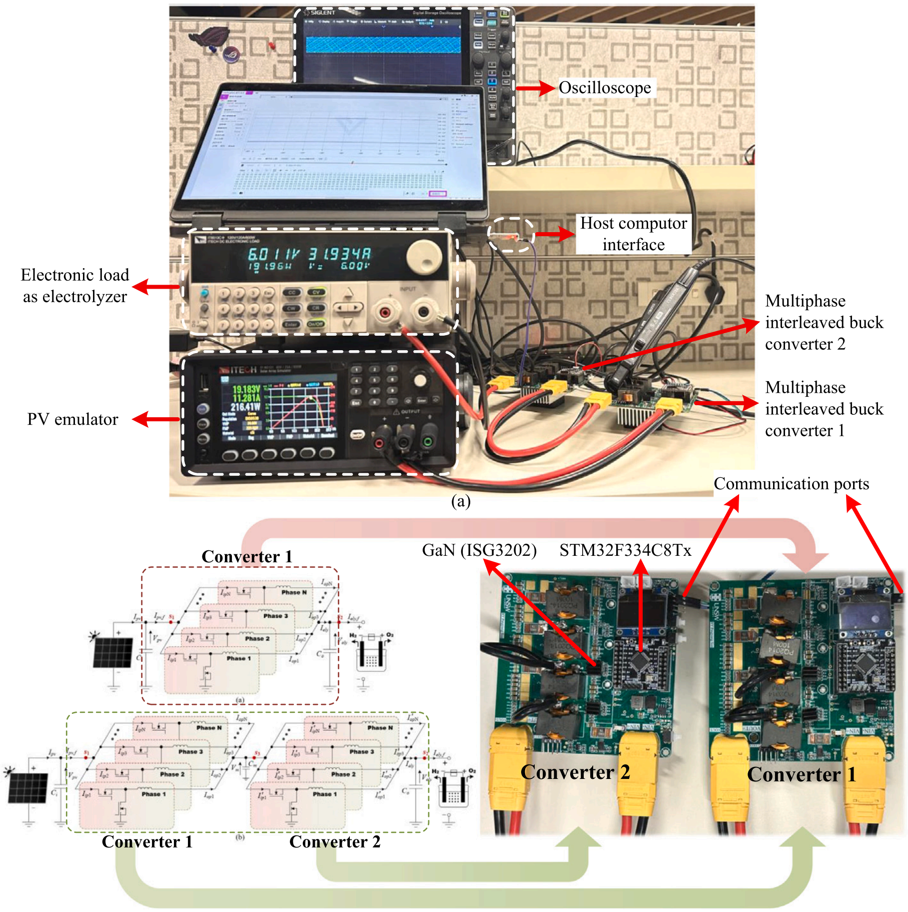

(a)

(b)

Fig. 13. Experiment platform of standalone PVEC system: (a) general platform with dual-converter configuration, and (b) converter hardware.

Table 6
Parameters of PV and emulated electrolyzer in the testing platform.

PV parameters		Electrolyzer parameters	
Maximum power P_{mp}	220 W	Rated power $P_{ely,rated}$	200 W
MPPT voltage V_{mp}	20 V	Rated voltage $V_{ely,rated}$	6 V
Open-circuit voltage V_{oc}	24.95 V	Rated current $I_{ely,rated}$	33.33 A
MPPT current I_{mp}	11.0 A	Number of cells N_{cell}	4
Short-circuit current I_{sc}	12.1 A	Reversible voltage V_{rev}	4.92 V

Table 7
Parameters of multiphase interleaved buck converters in the testing platform.

Input voltage range: 0–50 V	Output voltage range: 0–35 V
Input current range: 0–20 A	Output current range: 0–40 A
Inductor: $L = 10\ \mu$H	Equivalent input capacitor: $C_i = 156.4$ μF
Equivalent output capacitor: $C_o = 397.8$ μF	Equivalent middle capacitor*: $C_m = 554.2$ μF
Switching frequency: $f_s = 200$ kHz	Dead-time: 69.4 ns
MPPT tracking method: P&O	MPPT tracking update time: 200 ms
Allowable phase current difference: 0.1 A	Phase current correction coefficient: $c = 0.001$

* C_m is only present in the dual converter scheme, and $C_m = C_o + C_i$.

systems. By incorporating batteries or supercapacitors, the system can buffer short-term power fluctuations from the PV source while maintaining stable electrolyzer operation, or provide sufficient forward current to the electrolyzer during nighttime operation to prevent reverse current which could reduce cell lifetime.

6.2. *Adaptability to different electrolyzer technologies*

Beyond converter architecture, electrolyzer technology also affects the applicability of the proposed control framework. The present study focuses on PEM electrolyzers, as their fast dynamic response and wide partial-load operating range make them particularly suitable for the proposed converter control and LPRT strategies [4]. For broader deployment, however, technology-specific constraints must be considered when extending the proposed control method to other electrolyzer types.

For ALKs, the slower dynamic response and more restrictive low-load characteristics imply that the proposed ride-through strategy should respect stricter minimum-current and current-ramp constraints, especially in view of gas crossover and gas-purity limitations at low load [49, 50]. For SOECs, rapid operating transitions may induce significant thermo-mechanical stress because of the high operating temperature and the mismatch in thermal expansion among cell components; thus, any LPRT-oriented control transition would likely require additional filtering or thermal-state coordination [50]. By contrast, AEM is more amenable to the proposed control philosophy, as recent studies indicate that it is being actively explored for PV-coupled dynamic operation and can tolerate regular operational interruptions under properly managed conditions [4,51]. Therefore, the proposed LPRT strategies could in principle be adapted to AEM in a PEM-like manner. However, such adaptation should still employ more conservative start–stop and current-ramp management, and avoid prolonged operation at unfavorable

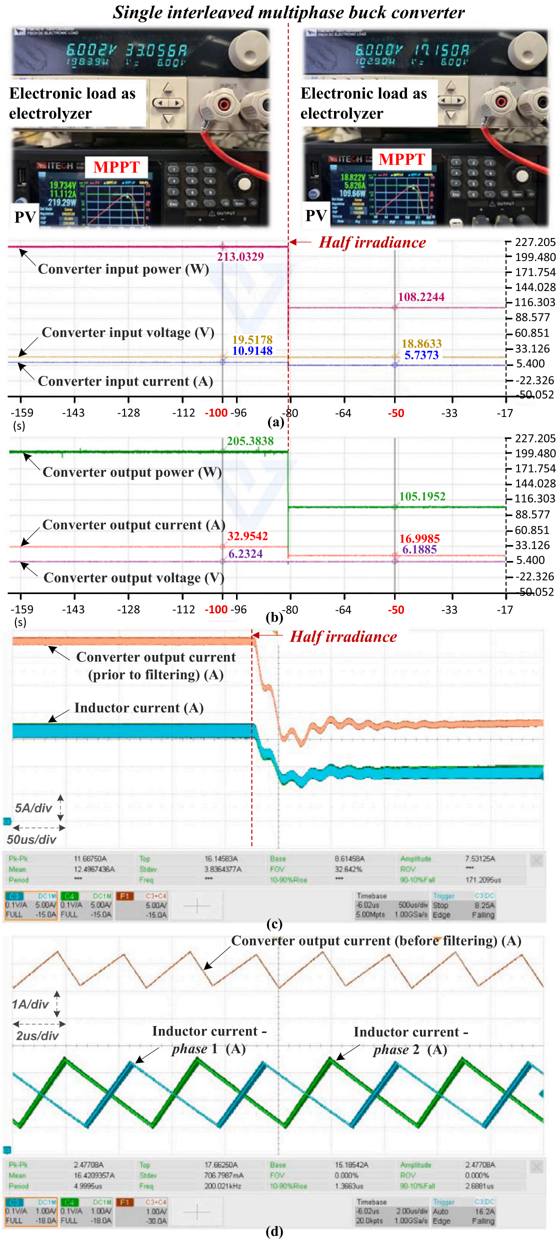

Fig. 14. Experimental results of standalone PVEC system with single-converter configuration.

low-current conditions, because AEM degradation under transient operation is strongly affected by operating conditions and current slope, while crossover during startup must also be carefully controlled [51]. Overall, although the proposed control framework is broadly relevant, its detailed implementation should remain technology-specific.

6.3. Converter solution comparison

The demonstrated interleaved buck converter used in standalone PVEC systems is cost-effective and highly efficient. Thanks to the multiphase configuration, it achieves high scalability and plug-and-play. In the future, the PVEC systems are expected to be more robust and standardized to achieve reliable long-term outdoor operation in sizes exceeding laboratory scale. Therefore, different dc/dc conversion technologies can be adopted to meet versatile operational requirements. For example, the dual-active-bridge (DAB) and triple-active-bridge (TAB) converters are promising candidates for achieving galvanic isolation and energy storage integration. For single-stage PVEC systems, the electrolyzer current ripple, PV open-circuit voltage and short-circuit current can be programmed in the MOPSO-based DAB parameter design which was proposed in [52] for improving PVEC's efficiency and power density. By implementing the proposed LPRT strategy, the partially rated TAB could be a high-efficiency isolated option for both single-stage and dual-stage systems, which is able to integrate energy storage and achieve fault isolation [53]. For MW-scale PVEC systems, a single-stage isolated dc/dc converter which consists of multiple resonant/non-resonant dc/ac cells with a multi-winding transformer unit can be considered [54,55]. Table 8 compares viable converter candidates that could be utilized in the proposed PVEC systems.

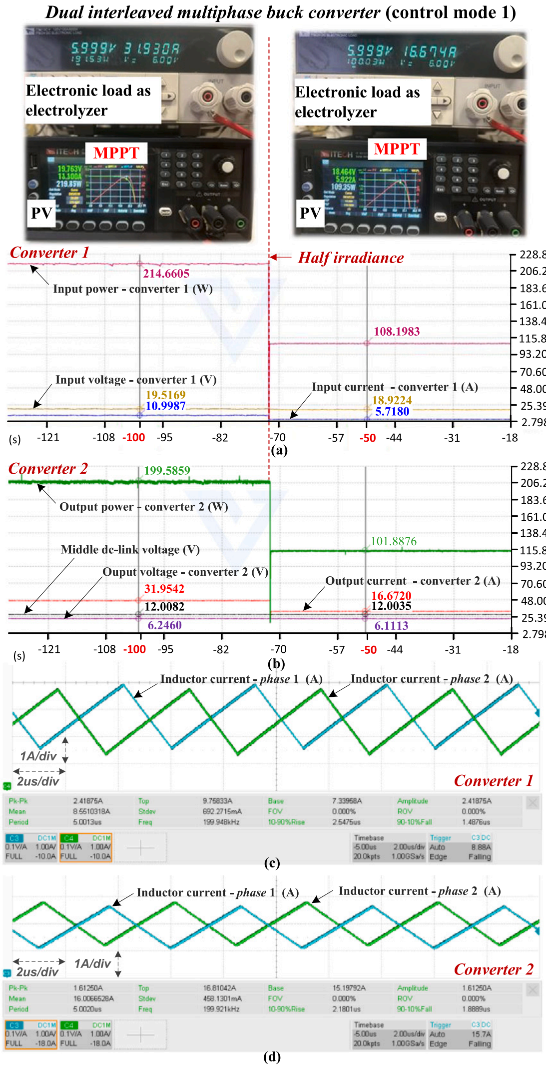

Fig. 15. Experimental results of standalone PVEC system with dual-converter under control mode 1.

6.4. Scheme scalability

When transitioning from laboratory prototypes to industrial scale PVEC installations, scalability and practical design considerations become increasingly important. For larger capacity systems with similar configurations, scalability can be achieved mainly by increasing the number of interleaved phases and appropriately scaling the PV array and electrolyzer stack ratings. The modular interleaved structure adopted in this work is inherently suitable for such extension, since each phase shares the output current and can be replicated using similar design

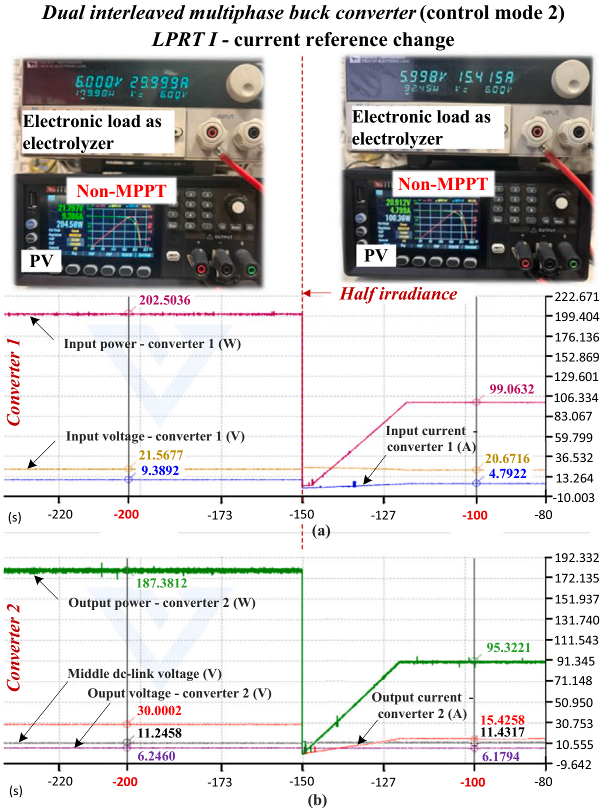

Fig. 16. Experimental results of a standalone PVEC system with a dual-converter under control mode 2 and LPRT Strategy I.

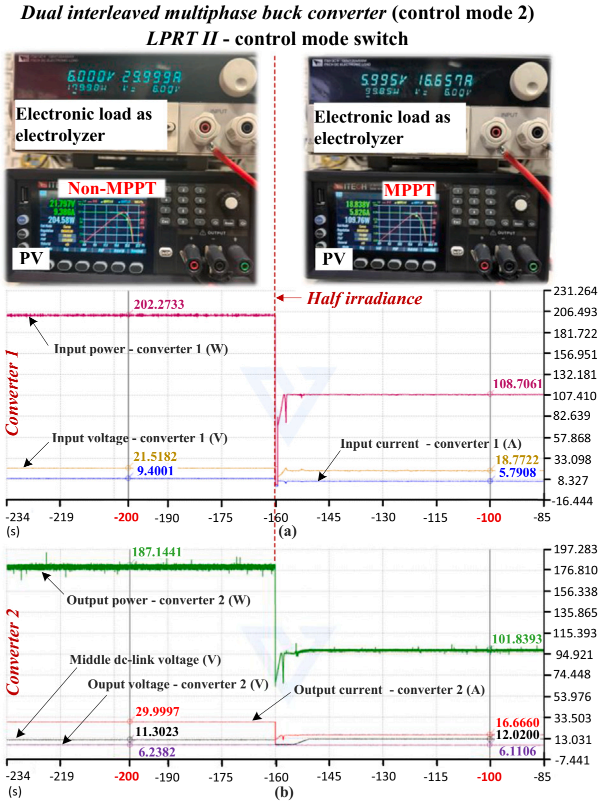

Fig. 17. Experimental results of standalone PVEC system with dual-converter under control mode 2 and LPRT Strategy II.

Table 8
Comparative converter solutions.

Type of dc/dc converter	Critical gain	Number of Components (S/D/T)	Efficiency	Ref.
Non-isolated single-stage	$\frac{2(N+1)}{1-\mathrm{D}}$	2/6/0	97%	[56]
Non-isolated dual-stage	$\frac{1}{N+1}$	2/6/0	N/A	[57]
Non-isolated dual-stage	$Z_{eq} = \sqrt{\frac{L_r L_a}{(L_r+L_a)C_r}}$	3/2/0	97.2%	[58,59]
Non-isolated single-stage	$\frac{2(N+1)}{1-\mathrm{D}}$	2/6/0	95.1%	[60]
Isolated single-stage	$\frac{V_{\mathrm{in}}}{N \cdot V_{out}}$	8/0/1	95.9%	[60]
Isolated dual-stage with battery	$N\left(\frac{\phi}{\pi} D(1-D)\right)$	4/6/1	96.8%	[61]

S: power switches; D: diodes; T: transformer.

principles. However, as system power increases, the voltage mismatch between the PV array and the electrolyzer limits the applicability of single stage configurations. In contrast, the dual stage architecture introduces an intermediate dc link, enabling independent PV MPPT and electrolyzer current control and thus better scalability for large scale PVEC systems. At higher power levels, additional engineering challenges such as thermal management, electromagnetic interference, and system level protection must also be carefully addressed, while the adoption of wide bandgap devices such as GaN or SiC can further improve switching performance and power density.

7. Conclusion

This work presents a system-level comparative study of single- and dual-stage dc/dc converter configurations for standalone PVEC systems, utilizing multiphase interleaved buck converters to address the application's high-current and large voltage-mismatch characteristics. Through detailed analysis of control strategies, comprehensive simulations, and hardware experiments, the study establishes key performance tradeoffs and provides validated design insights. The principal findings are summarized as follows:

(1) The single-stage configuration offers a simpler design but is fundamentally limited to a single degree of freedom, forcing the electrolyzer to passively follow the PV's maximum power point (electrolyzer-following mode). In contrast, the dual-stage configuration unlocks superior control flexibility, enabling decoupled regulation of the intermediate dc-link and the electrolyzer's dc current. This allows for precise control over hydrogen production, independent of solar availability, but within the maximum solar power output.

(2) The proposed LPRT strategies, including current reference change and control mode switch, are demonstrated to be effective in maintaining system stability for the dual-stage converter when operating in the electrolyzer current regulation mode. These strategies successfully prevent dc-link voltage collapse during sudden and significant solar power reductions, enhancing the system's operational resilience.

(3) The practical feasibility and high performance of both architectures and their respective control schemes are co-verified through simulation (5 kW) and experimental results on a 200 W GaN-based prototype. The experimental validation specifically confirms the high conversion efficiency and effective current sharing of the multiphase converters under various operating conditions.

These findings collectively indicate that while the single-stage converter is adequate for smaller-scale systems, the dual-stage architecture is not merely an option but a necessity for scaling up to industrial-level PVEC applications, where large voltage differentials make its staged conversion and advanced control capabilities indispensable. Furthermore, the intermediate dc-link in the dual-stage design serves as an ideal integration point for energy storage systems. This facilitates a transition from storage-less to storage-integrated systems, enabling fully dispatchable green hydrogen production by buffering power mismatches between the PV array and the electrolyzer. Future research can focus on the co-design and optimal energy management of hybrid storage systems (e.g., battery and supercapacitor) integrated at the dc-link, developing advanced control algorithms to maximize system efficiency and ensure on-demand hydrogen delivery.

CRediT authorship contribution statement

Pingyang Sun: Writing – original draft, Visualization, Validation, Software, Methodology, Investigation, Formal analysis, Data curation, Conceptualization. **Chunjun Huang:** Writing – original draft, Validation, Software, Investigation, Formal analysis, Conceptualization. **Hanwen Zhang:** Writing – original draft, Methodology, Investigation, Formal analysis, Data curation. **Zihang Qiu:** Validation, Investigation, Formal analysis, Data curation. **Shu Geng:** Validation, Investigation, Formal analysis. **Kaiwen Sun:** Writing – review & editing, Supervision, Project administration, Funding acquisition. **Xiaojing Hao:** Writing – review & editing, Supervision, Project administration.

Declaration of competing interest

The authors declare that they have no known competing financial interests or personal relationships that could have appeared to influence the work reported in this paper.

Acknowledgment

This work is supported by the Australia – UK Renewable Hydrogen Innovation Partnerships (GA396723), funded by the Department of Climate Change, Energy, the Environment and Water, Australian Government.

Data availability

No data was used for the research described in the article.

References

[1] Ouabi H, Lajouad R, Kissaoui M, El Magri A. Hydrogen production by water electrolysis driven by a photovoltaic source: a review. e-Prime - Adv Electr Eng Electron Energy 2024;8:100608.

[2] Zhao H, Yuan Z-Y. Progress and perspectives for solar-driven water electrolysis to produce green hydrogen. Adv Energy Mater 2023;13(16):2300254.

[3] Van LP, Hoang LH, Duc TN. A comprehensive review of direct coupled photovoltaic-electrolyser system: sizing techniques, operating strategies, research progress, current challenges, and future recommendations. Int J Hydrog Energy 2023;48(65):25231–49.

[4] Lopez VAM, Ziar H, Haverkort JW, Zeman M, Isabella O. Dynamic operation of water electrolyzers: a review for applications in photovoltaic systems integration. Renew Sustain Energy Rev 2023;182:113407.

[5] Australia PV Institute. Australian PV market since April 2001. https://pv-map.apvi.org.au/analyses.

[6] Yamane F. Fukushima hydrogen energy research field (fh2r). Toshiba Energy System and Solution Corporation; 2019.

[7] Li R, Jin X, Yang P, Sun X, Zhu G, Zheng Y, Zheng M, Wang L, Zhu M, Qi Y, Huang Z, Zhao L, Wang D, Yang W. Techno-economic analysis of a wind-photovoltaic-electrolysis-battery hybrid energy system for power and hydrogen generation. Energy Convers Manag 2023;281:116854. [Online]. Available: https://www.sciencedirect.com/science/article/pii/S0196890423002005.

[8] Hydrogeninsight. Chinese coal company starts construction on $600m Green hydrogen and methanol plant in northern China. https://www.hydrogeninsight.com/production/chinese-coal-company-starts-construction-on-600m-green-hydrogen-and-methanol-plant-in-northern-china/2-1-1733672.

[9] Gu X, Ying Z, Zheng X, Dou B, Cui G. Photovoltaic-based energy system coupled with energy storage for all-day stable PEM electrolytic hydrogen production. Renew Energy 2023;209:53–62.

[10] Astakhov O, Agbo SN, Welter K, Smirnov V, Rau U, Merdzhanova T. Storage batteries in photovoltaic–electrochemical device for solar hydrogen production. J Power Sources 2021;509:230367.

[11] Tello A, Cataño FA, Arunachalam A, Oyarzún D, Henriquez R, Valdivia P, Viswanathan MR, Gómez H. Green hydrogen production by photovoltaic-assisted alkaline water electrolysis: a review on the conceptualization and advancements. Int J Hydrog Energy 2025;107:378–95.

[12] Renaudineau H, Llor AM, Hernandez MS, Concha D, Wilson-Veas AH, Kouro S. Photovoltaic to electrolysis off-grid green hydrogen production with dc–dc conversion. Renew Energy 2024;237:121687.

[13] Abu Dhabi: International Renewable Energy Agency. IRENA. Green hydrogen cost reduction: scaling up electrolysers to meet the 1.5°c climate goal. Tech. Rep., 2020. [Online]. Available: https://www.irena.org/-/media/Files/IRENA/Agency/Publication/2020/Dec/IRENA_Green_hydrogen_cost_2020.pdf.

[14] Grigoriev SA, Fateev VN, Bessarabov DG, Millet P. Current status, research trends, and challenges in water electrolysis science and technology. Int J Hydrog Energy 2020;45(49):26036–58.

[15] LONGi Hydrogen. LONGi ALK g, 2025. [Online]. Available: https://www.longi.com/en/products/hydrogen/alk-g/.

[16] Laity E. Sungrow hydrogen launches green hydrogen production with hybrid electrolyser system, 2025. [Online]. Available: https://www.h2-view.com/story/sungrow-hydrogen-launches-green-hydrogen-production-with-hybrid-electrolyser-system/2125436.article/.

[17] Carmo M, Fritz DL, Mergel J, Stolten D. A comprehensive review on PEM water electrolysis. Int J Hydrog Energy 2013;38(12):4901–34.

[18] Satyapal S, Rustagi N, Green T, Melaina M, Penev M, Koleva M. Us National Clean hydrogen Strategy and roadmap. 2023.

[19] Sayedin F, Maroufmashat A, Sattari S, Elkamel A, Fowler M. Optimization of photovoltaic electrolyzer hybrid systems; taking into account the effect of climate conditions. Energy Convers Manag 2016;118:438–49.

[20] Khalilnejad A, Abbaspour A, Sarwat AI. Multi-level optimization approach for directly coupled photovoltaic-electrolyser system. Int J Hydrog Energy 2016;41(28):11884–94.

[21] Yang Z, Lin J, Zhang H, Lin B, Lin G. A new direct coupling method for photovoltaic module-pem electrolyzer stack for hydrogen production. Fuel Cells 2018;18(4):543–50.

[22] Coppitters D, De Paepe W, Contino F. Surrogate-assisted robust design optimization and global sensitivity analysis of a directly coupled photovoltaic-electrolyzer system under techno-economic uncertainty. Appl Energy 2019;248:310–20.

[23] Zhang W, Xu C. Capacity configuration optimization of photovoltaic-battery-electrolysis hybrid system for hydrogen generation considering dynamic efficiency and cost learning. Energy Convers Econ 2024;5(2):78–92.

[24] Mostafaeipour A, Rezayat H, Rezaei M. A thorough investigation of solar-powered hydrogen potential and accurate location planning for big cities: a case study. Int J Hydrog Energy 2020;45(56):31599–611.

[25] Reuß M, Reul J, Grube T, Langemann M, Calnan S, Robinius M, Schlatmann R, Rau U, Stolten D. Solar hydrogen production: a bottom-up analysis of different photovoltaic–electrolysis pathways. Sustain Energy Fuels 2019;3(3):801–13.

[26] Renaudineau H, Llor AM, Cortés R, Rojas CA, Restrepo C, Kouro S. Photovoltaic green hydrogen challenges and opportunities: a power electronics perspective. IEEE Ind Electron Mag 2021;16(1):31–41.

[27] Cai J, Weng C, Zhang R, Li Q, Zhang T, Shi Z. Comparative analysis on the dynamic operation performance of photovoltaic/thermal powered proton exchange membrane water electrolysis cogeneration system (pv/t-pemwe) under different connection modes. Renew Energy 2023;219:119566.

[28] García-Valverde R, Miguel C, Martínez-Béjar R, Urbina A. Optimized photovoltaic generator–water electrolyser coupling through a controlled dc–dc converter. Int J Hydrog Energy 2008;33(20):5352–62.

[29] Dahbi S, Aboutni R, Aziz A, Benazzi N, Elhafyani M, Kassmi K. Optimised hydrogen production by a photovoltaic-electrolysis system dc/dc converter and water flow controller. Int J Hydrog Energy 2016;41(45):20858–66.

[30] Li J, Li M, Zhang M, Qi R, Lin J. Design of a photovoltaic-to-hydrogen system for efficiency and safety under varying conditions. J Power Sources 2025;638:236487.

[31] Yodwong B, Guilbert D, Kaewmanee W, Phattanasak M, Hinaje M, Vitale G. Improved sliding mode-based controller of a high voltage ratio dc–dc converter for electrolyzers supplied by renewable energy. IEEE Trans Ind Electron 2023;71(8):8831–40.

[32] Guo X, Zhang S, Ding F, Zhu J, Bai H. A novel dc–dc converter for electrolyzer with low ripple and high step down. IEEE Trans Ind Electron 2024;71(10):12476–86.

[33] Lopez VAM, Isabella O, Zeman M, Ziar H. Battery-less uncertainty-based control of a stand-alone pv-electrolyzer system. J Power Sources 2024;614:234934.

[34] Chen W, Guo G, Huai Z, Liu B, Lan H. Dynamic modeling and control strategy optimization of photovoltaic-electrolyzer system via equivalent dynamic impedance. J Power Sources 2025;660:238554.

[35] Liu X, Zou J, Long R, Liu Z, Liu W. Variable period sequence control strategy for an off-grid photovoltaic-pem electrolyzer hydrogen generation system. Renew Energy 2023;216:119074.

[36] Sánchez-Squella A, Flores R, Burgos R, Morales F, Nader A, Valdivia-Lefort P. 99.6% efficiency dc-dc coupling for green hydrogen production using PEM electrolyzer, photovoltaic generation and battery storage operating in an off-grid area. Renew Energy 2024;237:121781.

[37] Lopez VAM, Ziar H, Zeman M, Isabella O. Maximization of PV energy use and performance analysis of a stand-alone PV-hydrogen system. Int J Hydrog Energy 2023;48(99):39298–314.

[38] Del Valle AG, García-Linares P, Martí A. Optimizing hydrogen production: a comparative study of direct and indirect coupling between photovoltaics and electrolyzer. Energy Convers Manag 2024;315:118751.

[39] Sanchez L, Reigosa D, Bilbao A, Peña-Gonzalez I, Briz F. Comparative analysis of power converter topologies for hydrogen electrolyzers. IEEE J Emerg Sel Top Power Electron 2024;12(5):4325–41.

[40] Shongwe S, Hanif M. Comparative analysis of different single-diode PV modeling methods. IEEE J Photovolt May 2015;5(3):938–46.

[41] Sera D, Mathe L, Kerekes T, Spataru SV, Teodorescu R. On the perturb-and-observe and incremental conductance MPPT methods for PV systems. IEEE J Photovolt Jul 2013;3(3):1070–8.

[42] Majumdar A, Haas M, Elliot I, Nazari S. Control and control-oriented modeling of PEM water electrolyzers: a review. Int J Hydrog Energy 2023;48(79):30621–41.
[43] Olivier P, Bourasseau C, Bouamama PB. Low-temperature electrolysis system modelling: a review. Renew Sustain Energy Rev 2017;78:280–300.
[44] Ratib MK, Muttaqi KM, Islam MR, Sutanto D, Agalgaonkar AP. Electrical circuit modeling of proton exchange membrane electrolyzer: the state-of-the-art, current challenges, and recommendations. Int J Hydrog Energy 2024;49:625–45.
[45] Martinson CA, Van Schoor G, Uren KR, Bessarabov D. Characterisation of a PEM electrolyser using the current interrupt method. Int J Hydrog Energy 2014;39(36):20865–78.
[46] Roth Jr CH. Latches and flip-flops. Boston: PWS: Fundamentals of Logic Design.; 1995.
[47] GoodWe. GoodWe Polaris series. https://en.goodwe.com/polaris-series.
[48] Sun P, Wang Y, Khalid M, Blasco-Gimenez R, Konstantinou G. Steady-state power distribution in VSC-based MTDC systems and DC grids under mixed p/v and i/v droop control. Elect Power Syst Res 2023;214:108798.
[49] Nnabuife SG, Hamzat AK, Whidborne J, Kuang B, Jenkins KW. Integration of renewable energy sources in tandem with electrolysis: a technology review for green hydrogen production. Int J Hydrog Energy 2025;107:218–40.
[50] Wang J, Yang J, Feng Y, Hua J, Chen Z, Liao M, Zhang J, Qin J. Comparative experimental study of alkaline and proton exchange membrane water electrolysis for green hydrogen production. Appl Energy 2025;379:124936.
[51] Gladik A, Riedel M, Eichel R-A. Anion exchange membrane electrolysis at work—investigating impact of starting parameters and start–stop operation on cold start behavior and degradation. J Power Sources 2025;628:235878.
[52] Ren H, Zhang H, Wang Y, Yu H, Sun P, Chen Z. A multidimensional design for dual active bridge converters in low-voltage DC systems. IEEE Trans Ind Electron 2026;73(2):2264–75.
[53] Zhang H, Yu H, Sun P, Zhu X, Zhang Q, Wang Y, Bifaretti S, Qin Z, Li G, Chen Z. A partially rated interlinking converter with distributed energy storage for active power sharing in DC microgrids. IEEE Trans Power Electron 2025;40(7): 9370–87.
[54] Zhang H, Wang Y, Yu H, Chen Z. A novel flexible multiport interlinking converter for DC microgrid clusters. IEEE Trans Ind Appl 2024;60(2):2901–13.
[55] Chunming Y, Peter S, Adrian T, Philippe M, Juergen STEINKE, Stephane I, Ralph B. A novel flexible multiport interlinking converter for DC microgrid clusters, vol. 20230318435A1. United States Patent Application Publication; 2024.
[56] Tseng K-C, Huang C-C. High step-up high-efficiency interleaved converter with voltage multiplier module for renewable energy system. IEEE Trans Ind Electron 2014;61(3):1311–9.
[57] Zhu Y, Yang X, Wang M, Mu W, Liu Y, Zheng TQ, Li S. Fault protection and control strategy of multilevel voltage-balancing dc-dc converter. IEEE Trans Ind Appl 2024;60(1):596–607.
[58] Faraji R, Ding L, Rahimi T, Kheshti M. Application of soft-switching cell with inherent redundancy properties for enhancing the reliability of boost-based dc–dc converters. IEEE Trans Power Electron 2021;36(11):12342–54.
[59] Martins MLS, Hey HL. Self-commutated auxiliary circuit Zvt PWM converters. IEEE Trans Power Electron 2004;19(6):1435–45.
[60] Li W, Zhao Y, Wu J, He X. Interleaved high step-up converter with winding-cross-coupled inductors and voltage multiplier cells. IEEE Trans Power Electron 2012;27(1):133–43.
[61] Wu H, Sun K, Zhu L, Xing Y. An interleaved half-bridge three-port converter with enhanced power transfer capability using three-leg rectifier for renewable energy applications. IEEE J Emerg Sel Top Power Electron 2016;4(2): 606–16.